Numerical simulations of stochastic partial differential equations for extreme rainfall, large-scale circulations and climate change

by
Tianhong Huang

A dissertation submitted in partial fulfillment
of the requirements for the degree of
Doctor of Philosophy
Mathematics

at the
University of Wisconsin-Madison
2023

Date of Final Oral Exam: 04/20/2023
The dissertation is approved by the following members of the Final Oral Committee:

Samuel Stechmann, Professor, Mathematics
Leslie M. Smith, Professor, Mathematics
Nan Chen, Associate Professor, Mathematics
Larissa E Back, Associate Professor, Atmospheric & Ocean Science

Numerical simulations of stochastic partial differential equations for extreme rainfall, large-scale circulations and climate change

Tianhong Huang

Abstract

Climate change is a pressing global issue that has spurred intense scientific research to understand its various aspects. In climate predictions, clouds are the leading source of uncertainty. This is partly because, to simulate the fluid dynamics of climate over the entire globe, a large grid spacing must be used, so clouds are a subgrid-scale parametrization rather than a resolved feature. Simple models have been valuable for understanding clouds and climate feedbacks, and also for cloud and rainfall statistics. However, simple models typically represents one of these respects but not both, either cloud statistics in a single region, rather than globally, or climate over a large region but without individual clouds and their statistics. Here a framework of stochastic model is investigated with clouds evolving in a planetary-scale domain with different regions, such as a warm-pool region with prominent deep convective clouds and a cold-pool region with prominent stratocumulus clouds and little or no deep convection. The spatiotemporal stochastic clouds are interactively coupled with an idealized climate system, with simplified vertical structure being used and the full fluid dynamics of cloud circulations not resolved. Nevertheless, the types of clouds (deep convective clouds and boundary-layer clouds such as shallow cumulus and stratocumulus clouds), lifetimes, and sizes of clouds are all interactive and coupled with an idealized Walker circulation. In addition, other basic aspects of the idealized climate system like interactive radiation with water vapor and cloud feedbacks are included. With these ingredients (evolving clouds, planetary-scale circulations and radiation), the framework takes the ability for idealized investigations of climate change with increased quantity of carbon dioxide and changes in the statistics of extreme rainfall events and stratocumulus cloud decks under different longwave absorptivity conditions. In this thesis, the formulation of the model equations is presented, and numerical simulations are shown to illustrate the model dynamics and climate changes. The climate sensitivity of model results to various cloud microphysical properties such as aerosols amount is also examined.

Dedication

This thesis is dedicated to my parents and beloved orange cat, Jinggai. Who instilled in me a love of learning and a passion of science, and who have always been there for me through thick and thin; whose presence and companionship have brought joy and comfort to my life, your purrs, snuggles, and playful antics provided a welcome distraction and helped me stay grounded. Thank you all for being my rock, my partner, and my inspiration. This thesis is dedicated to you.

Declaration

I declare that this thesis, entitled "Numerical simulations of stochastic partial differential equations for extreme rainfall, large-scale circulations and climate change", represents my own work, conducted under the supervision of Prof. Samuel N. Stechmann. The research was conducted in accordance with the University's guidelines on academic intergrity and research ethics, and all sources used in the preparation of this thesis have been appropriately cited and acknowledged.

Furthermore, I declare that this work has not been submitted in whole or in part for any other degree or qualification at this or any other instituition. I understand that any attempt to pass off someone else's work as my own, or any other form of academic misconduct, will result in severe penalties, including the possibility of revocation of my degree.

Acknowledgements

I would like to express my deepest gratitude to my advisor, Prof. Stechmann, for his invaluable guidance, support, and encouragement throughout this research. His expertise, insights, and feedback were instrumental in shaping the direction and focus of this thesis, and I am truly grateful for his mentorship.

I would also like to thank the members of my thesis committee, Prof. Smith, Prof. Chen and Prof. Back, for their thoughtful feedback and valuable input during the development of this work.

I am indebted to my colleagues, for their support, camaraderie, and providing advice were instrumental in shaping my thinking. To my close friends, Chun, Yu, Shuqi and Hongxu, whose support and encouragement were invaluable in helping me navigate the ups and downs of graduate school life. Thank you for your thoughtful feedback, your willingness to listen, and your unwavering support, even during the toughest times.

I would like to extend a special thanks to my spouse, Yunqi, whose love and support have been a constant source of strength and inspiration. Her encouragement to keep going, even when things were though, were instrumental in my ability to complete this research. Their love, understanding, and patience have been a lifeline during the many long hours of research and writing, and I am grateful for their unwavering belief in me.

Finally, I would like to express my gratitude to the funding agencies and organizations that supported this research, including a Vilas Associate Award that was awarded to Prof.Stechmann from the University of Wisconsin-Madison Office of the Vice Chancellor for Research and Graduate Education with funding from the Wisconsin Alumni Research Foundation.

Contents

List of Figures

List of Tables

Chapter 1

Introduction

Global climate is influenced by both radiation and fluid dynamics. In the simplest models of climate, radiative transfer alone can be used to illustrate basic principles, such as the greenhouse effect due to carbon dioxide [1]. However, for more precise predictions of climate, the combined effects of radiation and atmospheric/oceanic fluid dynamics are needed, as in, for instance, contemporary global climate models (GCMs) [2, 3].

In GCM predictions of future climate change, the leading source of uncertainty is clouds [4–7]. Clouds can potentially have either a cooling effect or a warming effect. By reflecting solar radiation, clouds can have a cooling effect. On the other hand, clouds can absorb the radiation that is emitted by the earth's surface, and, in so doing, can produce a greenhouse warming effect in much the same way as carbon dioxide. Furthermore, different types of clouds (see Fig. 1.1) can have different effects on climate. For instance, shallow clouds near the earth's surface end to have a greater cooling effect than warming effect. On the other hand, the deep clouds of a thunderstorm have both cooling and warming effects, and the cooling and warming effects can cancel each other and result in a near-zero impact on the radiation budget.

Moreover, it is important to emphasize that the difficulty is not only the clouds themselves but also their interaction with large-scale atmospheric fluid dynamics [2–7]. As illustrated in Fig. 1.1, different cloud types are associated with different components of large-scale circulations. For instance, deep convective clouds are associated with the ascending branch of the Walker circulation, and shallow clouds are associated with the descending branch. Hence the two phenomena—clouds and circulation—are inextricably linked, and uncertainties related to clouds are also uncertainties related to cloud–circulation interactions.

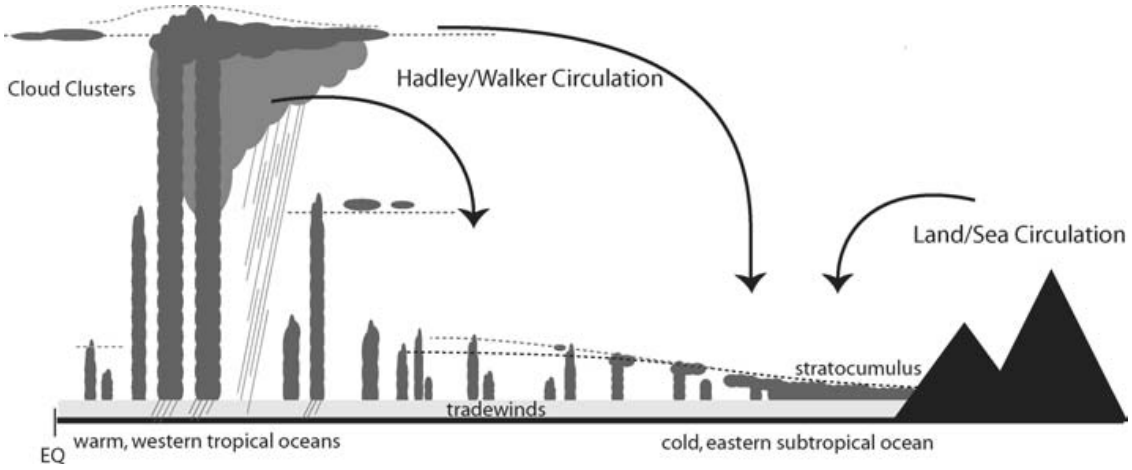

Figure 1.1: Schematic diagram of cloud regimes and associated large-scale circulations. Deep convective clouds are associated with the ascending branch of the Walker circulation, and shallow clouds are associated with the descending branch of the Walker circulation. From Ref. [8]. Used with permission.

To properly account for the effects of clouds on climate, one would like to perform numerical simulations of atmospheric fluid dynamics. However, a major challenge is that clouds and climate operate across a vast range of scales. In Fig. 1.1, the small-scale features include shallow cumulus and stratocumulus clouds, which require a grid spacing of $O(100)$ m or $O(10)$ m or smaller in large eddy simulations (LES) [9–12]. On the large scales, on the other hand, is the Walker circulation, which spans scales of $O(10^6)$ or $O(10^7)$ m [13, 14]. For such a vast range of scales, LES or cloud-resolving models (CRMs) are computationally expensive. On a more limited scale, CRMs have been used to explore clouds, precipitation, and climate change, although typically only over a limited

area on regional scales and not including large-scale circulations [15–18]. If restricted to 2D, a CRM could go as far as to simulate a Walker circulation and deep convection [19], although to also resolve stratocumulus clouds would be computationally expensive. Typically, to include large-scale circulations such as the Walker circulation, GCMs can be used, although the grid spacing is typically $O(10^4)$ or $O(10^5)$ m, which is too large to resolve individual clouds, so clouds are parameterized as a subgrid-scale process [2, 3] or resolved on fine scales as part of a multi-scale modeling framework [20]. In summary, due to computational expense, it is difficult to simultaneously simulate the full range of important scales in Fig. 1.1, from large-scale circulations to the individual cloud features of shallow clouds such as stratocumulus clouds.

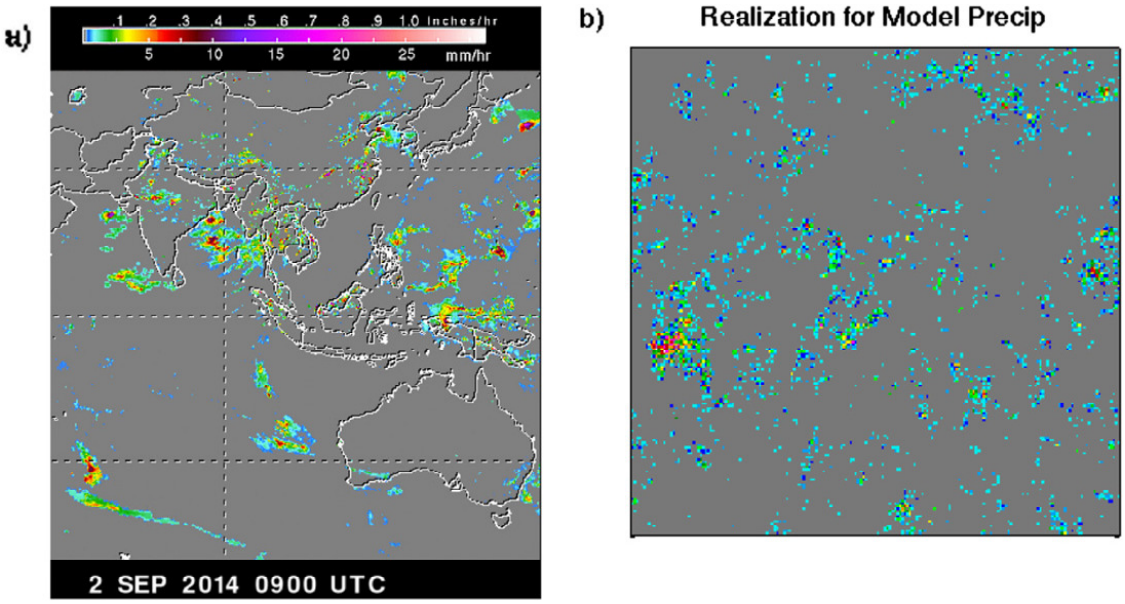

Figure 1.2: Comparison of precipitation from (a) observational data and (b) stochastic model. Note that a stochastic model will not reproduce the exact same locations of individual cloud clusters in observational data on a particular day. The statistics, though, can be compared and are similar (in terms of, for instance, power spectral density and the pdf of cloud cluster area). From Ref. [21]. © American Meteorological Society. Used with permission.

The goal of the present thesis is to investigate another modeling framework, in addition to LES, CRMs, and GCMs, as a way of potentially simulating both large-scale circulations and shallow clouds such as stratocumulus clouds. The idea is to use

a stochastic model for the spatiotemporal variability of clouds. Example snapshots from stochastic models are shown in Figs. 1.2 and 1.3 for deep convective and shallow clouds, respectively, to illustrate the level of statistical realism. Many cloud statistics can be simulated by stochastic models [21–25], including different regimes of shallow clouds such as stratocumulus clouds, which have been identified as the main contributor to cloud feedback uncertainties in GCM climate predictions [6]. Here, a stochastic model for shallow clouds [22] will be combined with a model for deep convection and large-scale atmospheric fluid dynamics [26–32], thereby encompassing the phenomena in Fig. 1.1, from shallow clouds on small scales to the Walker circulation on large scales.

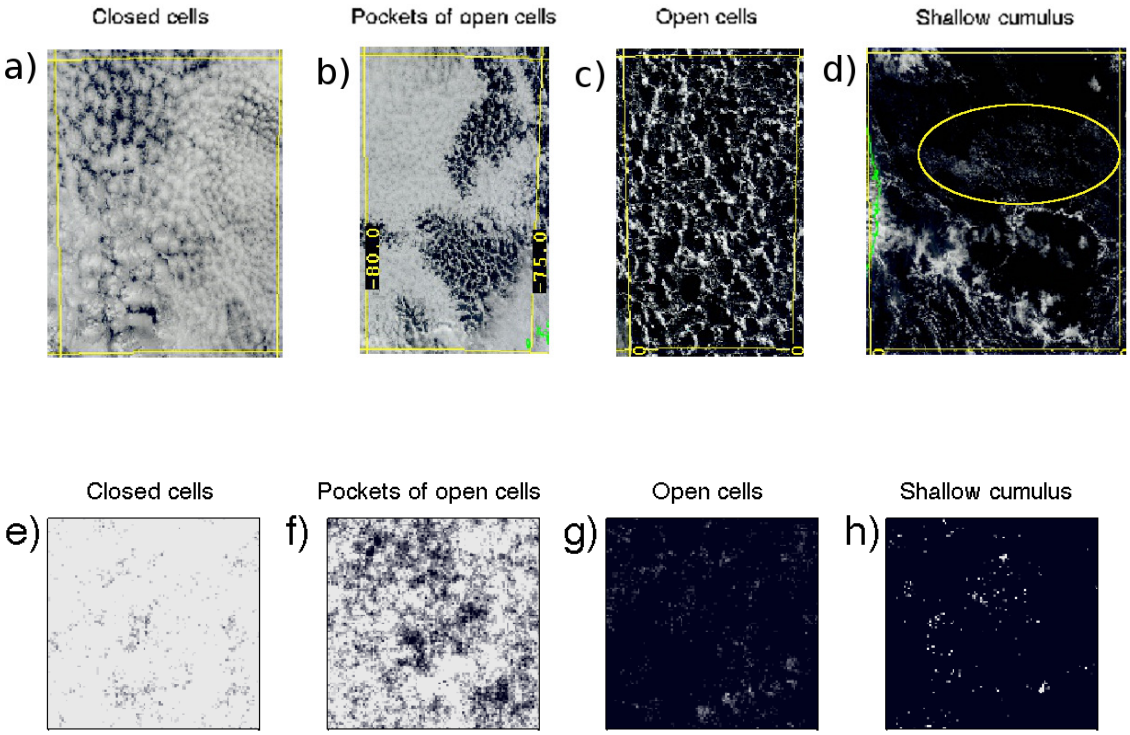

Figure 1.3: Stochastic model representation [panels (e)–(h)] of four types of shallow cloud organization, as seen from satellite in panels (a)–(d). Yellow lines indicate areas of 5° longitude by 5° latitude. The model domain size is also 5° by 5°. From Ref. [22]. Used with permission.

A significant computational savings can be achieved by using stochastic models instead of LES. The computational savings comes in part from an increase in horizontal grid spacing, since LES of stratocumulus clouds would require a horizontal grid spacing

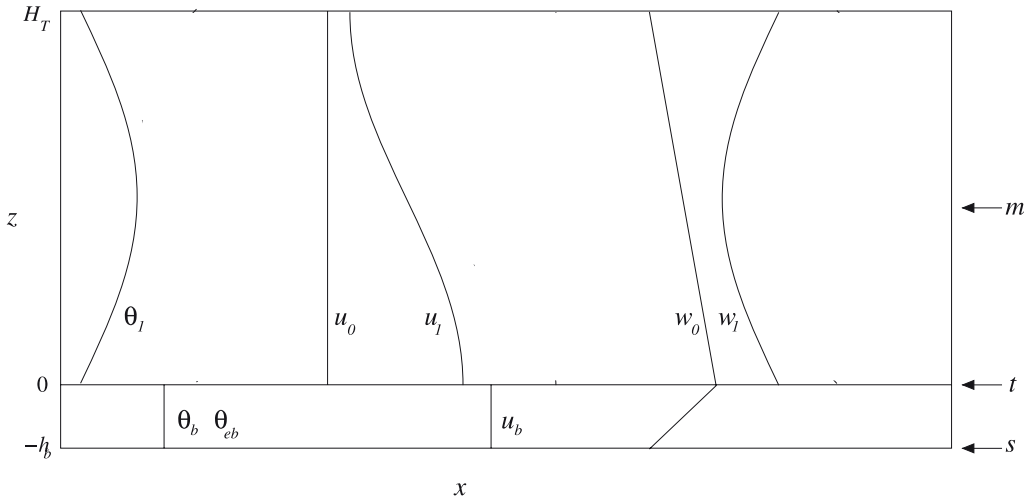

Figure 1.4: Schematic diagram of the vertical structures of the atmospheric model variables. The height labels s, t, and m correspond to the surface of the earth, the top of the atmospheric boundary layer, and the mid-troposphere. Adapted from Ref. [35]. © American Meteorological Society. Used with permission.

of $O(10)$ or $O(100)$ m, whereas the stochastic models can use a horizontal grid spacing of $O(10^3)$ or $O(10^4)$ m. In addition, the vertical grid also provides a significant computational savings, since LES of stratocumulus clouds would require a vertical grid spacing of $O(10)$ or $O(100)$ m, whereas the stochastic models use simplified vertical structures, as illustrated in Fig. 1.4. The vertical structures in Fig. 1.4 arise from a Sturm–Liouville problem from the equations for atmospheric fluid dynamics [33, 34], and they are also the basic vertical structures associated with the deep convective clouds and Walker circulation in Fig. 1.1. As a result of the simplified vertical structure, the stochastic models have a computational grid with the number of dimensions reduced by one, from a three-dimensional (3D) grid to a two-dimensional (2D) grid.

With atmospheric fluid dynamics partially represented, the present framework is intermediate in complexity between, on the one hand, LES/CRM/GCM frameworks, and, on the other hand, simplified models such as two-box models that do not resolve detailed structures of atmospheric circulations (see Refs. [36, 37] and references therein). While a two-box model can represent the widths of entire regions (such as one single grid box for the entire ascending branch of the Walker circulation and another grid box for the

descending branch), the present framework can furthermore represent individual cloud clusters within those regions. It is also possible, within LES/CRM/GCM frameworks, to simulate both shallow clouds and large-scale circulations by using mesh refinement or grid stretching, which has been explored in a variety of different configurations [38–41], although at significant computational expense. While the present stochastic framework is idealized in comparison to LES/CRM/GCM frameworks, the stochastic framework brings a large computational savings that can be invested in, for instance, faster exploration of parameter space and larger ensembles of simulations.

In this thesis, the vertical structure together with physical descriptions of model variables and equations are presented in Chap. 2, the numerical method and parallel framework are described in Chap. 3, numerical simulations and individual statistics are illustrated in Chap. 4, and conclusions are summarized in Chap. 5.

Chapter 2

Model description

In this chapter, the model variables and equations are described. The basic components of the fluid dynamics are similar to other models [26–32, 35, 42–46] that have used simplified vertical structures as in Fig. 1.4. One main new aspect here is the inclusion of stochasticity as in recent work [21–25] so that the stochastic models for shallow clouds and cloud clusters are extended to be coupled with radiation and large-scale atmospheric fluid dynamics, and large-scale fluid dynamics. Another new aspect is that some parameterizations (such as mixing of water at the top of the cloudy boundary layer) need to be adapted for use with the smaller grid spacings of $O(5)$ km here in comparison to larger grid spacings in earlier work. In what follows, the model variables are described in section 2.1; the evolution equations are described in sections 2.2, 2.3, 2.4, and 2.5, for the free troposphere, barotropic modes, boundary layer, and ocean, respectively.

2.1 Model variables and vertical structures

The model variables will have simplified vertical structures, as illustrated in Fig. 1.4, which brings a substantial savings in computational cost. Note that the functional form of the vertical structures arises systematically from a Sturm–Liouville problem [33], and

the simplification (and computational savings) comes from using a superposition of only two vertical modes rather than an infinite sum of vertical modes.

2.1.1 Vertical structures and velocities

The form of the vertical structures can be derived from a Sturm–Liouville problem associated with the linearized evolution equations. The subscript f indicates that the variables are associated with the free troposphere, where the components of the velocity vector are u_f, v_f, and w_f, and the other variables are the (scaled) pressure p_f, potential temperature θ_f, and water vapor mixing ratio q_f.

$$\frac{\partial u_f}{\partial t} + \frac{\partial p_f}{\partial x} = 0, \tag{2.1}$$

$$\frac{\partial v_f}{\partial t} + \frac{\partial p_f}{\partial y} = 0, \tag{2.2}$$

$$\frac{\partial p_f}{\partial z} = g\frac{\theta_f}{\theta_f^{ref}}, \tag{2.3}$$

$$\frac{\partial u_f}{\partial x} + \frac{\partial v_f}{\partial y} + \frac{\partial w_f}{\partial z} = 0, \tag{2.4}$$

$$\frac{\partial \theta_f}{\partial t} + w_f\frac{\partial \theta_{bg}}{\partial z} = 0, \tag{2.5}$$

$$\frac{\partial r_f}{\partial t} + w_f\frac{\partial r_{bg}}{\partial z} = 0. \tag{2.6}$$

The equations in (2.1)–(2.6) are a linearization of the hydrostatic Boussinesq equations, also known as the primitive equations. Evolution equations will be discussed in further detail below. For the moment, the evolution equations are introduced in (2.1)–(2.6) to explain the form of the vertical structures. In particular, in seeking solutions of (2.1)–(2.6) based on separation of variables, a Sturm–Liouvile problem arises for the vertical structures [33]. Let $G_j(z)$, for $j = 0, 1, 2, 3, \cdots$, denote the vertical basis functions that arise from the Sturm–Liouville problem. A generic variable $\phi(x, y, z, t)$ can then be

expressed as an infinite series as

$$\phi(x,y,z,t) = \sum_{j=0}^{\infty} \phi_j(x,y,t) G_j(z), \tag{2.7}$$

where the functions $\phi_j(x,y,t)$ are the expansion coefficients. For simplified models, it is common to truncate the infinite series after the first terms as, for instance,

$$\phi(x,y,z,t) \approx \phi_0(x,y,t) G_0(z) + \phi_1(x,y,t) G_1(z). \tag{2.8}$$

These first two terms are called the barotropic mode and the first baroclinic mode, respectively. It is common to consider such a truncation since it embodies the essential features of atmospheric circulation [26–28, 47–51] and since the first terms contain the most variability based on observational data analyses [52, 53]. For a Boussinesq system, the basis functions $G_j(z)$ are sines and cosines [33], as described in further detail next.

In the free troposphere, the three-dimensional velocity vector is partitioned into its two-dimensional horizontal component, $\mathbf{u}_f = (u_f, v_f)$, and its vertical component, w_f, with subscript f to denote the free troposphere. For velocity, the expansion from (2.8) takes the form

$$\mathbf{u}_f(x,y,z,t) = \mathbf{u}_0(x,y,t) + \mathbf{u}_1(x,y,t)\sqrt{2}\cos\frac{\pi z}{H_T}, \tag{2.9}$$

$$w_f(x,y,z,t) = w_0(x,y,t)(H_T - z) + w_1(x,y,t)\sqrt{2}\sin\frac{\pi z}{H_T}, \tag{2.10}$$

where H_T is the depth of the troposphere, and these vertical structures of $\sin(\pi z/H_T)$ and $\cos(\pi z/H_T)$ arise from a Sturm–Liouville problem [33], under the assumption of a Boussinesq atmosphere. For a Boussinesq system, the incompressibility

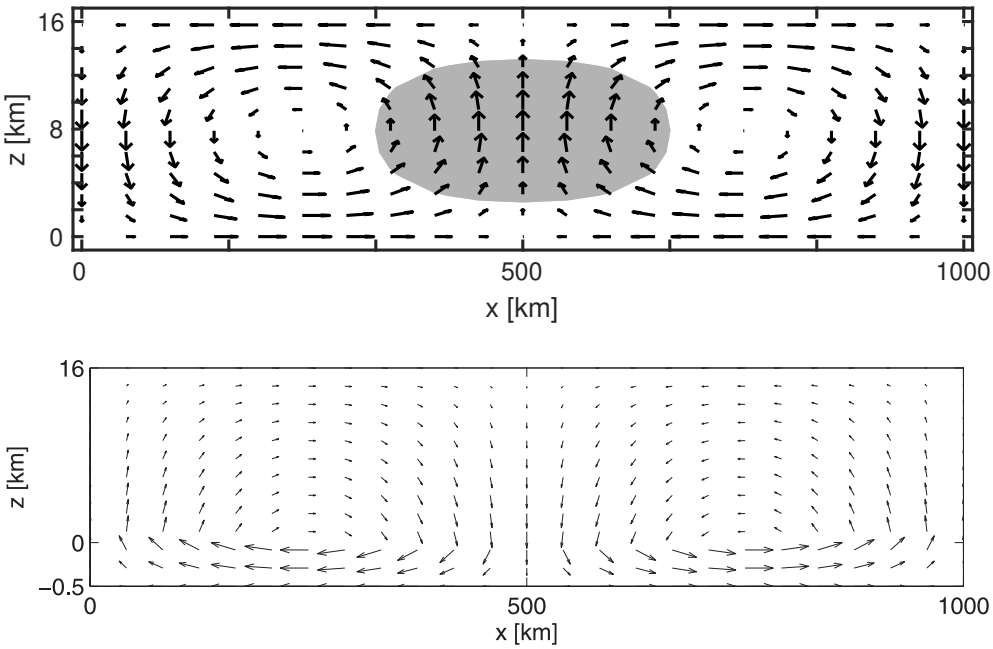

Figure 2.1: Illustrations of circulation cells that arise from the vertical structures from Fig. 1.4. Top: A deep circulation cell arises from u_1 and w_1. Gray shading indicates deep convective clouds associated with upward motion, as in the Walker circulation cells of Fig. 1.1. Bottom: Boundary-layer convergence from u_b can create a circulation cell in concert with free-tropospheric, barotropic u_0, w_0. Bottom panel is from Ref. [35].

condition of $\partial_x u_f + \partial_y v_f + \partial_z w_f = 0$ leads to the equations

$$(\partial_x u_0 + \partial_y v_0 - w_0) + (\partial_x u_1 + \partial_y v_1 + \frac{\pi}{H_T} w_1)\sqrt{2}\cos\frac{\pi z}{H_T} = 0. \tag{2.11}$$

After pairing corresponding terms would induce the relationships between vertical velocity and horizontal component

$$w_0 = \partial_x u_0 + \partial_y v_0, \qquad w_1 = -\frac{H_T}{\pi}(\partial_x u_1 + \partial_y v_1). \tag{2.12}$$

If an anelastic atmosphere is assumed instead of Boussinesq, then the vertical gradient of density is taken into account, and the vertical structures have a more complicated form [26], although in either case the basic features are the same. One could include additional basis functions [29, 34], such as $\sin(2\pi z/H_T)$ or $\sin(3\pi z/H_T)$, etc., beyond the first baroclinic mode structure $\sin(\pi z/H_T)$ used here, but the largest amount of atmospheric variance is in the first baroclinic mode [52]. As an illustration, if the velocity structures in (2.9)–(2.10) are plotted as vector fields, then a sinusoidal variation in x will produce a circulation cell as shown in Fig. 2.1. The deep circulation cell in Fig. 2.1 is similar to the Walker circulation cells from Fig. 1.1, which indicates that the simple vertical structures in (2.9)–(2.10) are sufficient to capture the basic aspects of deep convection and atmospheric circulations.

2.1.2 Thermodynamic variables of free troposphere

The thermodynamic variables in the free troposphere are the potential temperature, θ_f, and the water vapor mixing ratio, r_f. Their structures take the form

$$\theta_f(x,y,z,t) = \theta_f^{ref} + \theta_{bg}(z) + \theta_1(x,y,t)\sqrt{2}\sin\frac{\pi z}{H_T}, \tag{2.13}$$

$$r_f(x,y,z,t) = r_0(x,y,t)e^{-z/H_q}, \tag{2.14}$$

Table 2.1: Layer parameters and thermodynamic parameters

parameters	value	unit	description
H_T	15500	m	Tropopause height
h_b	1000	m	Atmospheric boundary layer thickness
h_o	10	m	Ocean mixed layer thickness
ρ_o	1000	kg/m^3	Density of ocean water
ρ_b	0.885	kg/m^3	Density of boundary layer air
ρ_f	0.37	kg/m^3	Density of free troposphere air
c_o	4148	J/kg/K	Heat capacity of ocean water
c_p	1005	J/kg/K	Heat capacity of dry air
R_d	287	J/kg/K	Gas constant of dry air
L_v	2.4×10^6	J/kg	Latent heat of vaporization

which are similar to (2.9)–(2.10). In (2.13), θ_f^{ref} is a constant reference value, and $\theta_{bg}(z)$ is a background profile, with $\theta_{bg}(0) = 0$ and with $d\theta_{bg}/dz$ a positive constant. In (2.14), H_q is a decay height for the moisture profile, and r_0 is the value at the top of the boundary layer, $z = 0$. Layer parameters and thermodynamic parameters are listed in Table 2.1, and parameter values of the background states are listed in Table 2.2.

In addition to the mixing ratio r_f, it is also sometimes convenient to work with the column water vapor (CWV), which we denote by q_f and define as

$$q_f(x, y, t) = \frac{\rho_f}{\rho_o} \int_0^{H_T} r_f(x, y, z, t)\, dz, \tag{2.15}$$

which is the integral of the mixing ratio over the atmospheric column. The density ρ_f is the average density of the atmosphere in the free troposphere, and it could be replaced by a height-dependent $\tilde{\rho}(z)$ and brought inside the integrand, although the version in (2.15) will serve the present purposes. The parameter ρ_o is the density of liquid water (or ocean water), and one can see that (2.15) transforms r_f with units of kg water per kg dry air (or kg kg^{-1} for short) to q_f with units of mm. Physically, the CWV q_f represents the height

of liquid water that would result if all water vapor in the column were condensed to liquid form.

Since both $r_0(x, y, t)$ from (2.14) and $q_f(x, y, t)$ from (2.15) will be useful in different contexts, it is helpful to define the relationship between them. To do so, insert (2.14) into (2.15) to find

$$q_f = H_T \hat{Q}_0 \frac{\rho_f}{\rho_o} r_0, \quad \text{with} \quad \hat{Q}_0 = \frac{H_q}{H_T}\big(1 - \exp(-H_T/H_q)\big). \tag{2.16}$$

For short, we will sometimes refer to the water vapor mixing ratio (r_f or r_0) or the column water vapor as simply the "water" or the "moisture."

In addition to the potential temperature θ_f, it is also useful to define other temperature quantities. The temperature itself will be denoted by T_f^{tot} to indicate that it is the total temperature as opposed to an anomaly, and it is related, by definition, to potential temperature via

$$T_f^{tot}(x, y, z, t) = \theta_f(x, y, z, t) \cdot \left(\frac{\tilde{p}(z)}{p_0}\right)^{R_d/c_p} \tag{2.17}$$

where R_d is the gas constant for dry air, c_p is the specific heat at constant pressure, $\tilde{p}(z)$ is the background pressure profile, and p_0 is a reference pressure that is taken to be the surface pressure—i.e., $p_0 = \tilde{p}_f(0)$.

For later use with radiative transfer, with simplified vertical structures, it is convenient to define the mass average of the temperature in the free troposphere, which we will call T_f:

$$T_f = \frac{1}{\int_0^{H_T} \tilde{\rho}(z) dz} \int_0^{H_T} T_f^{tot}(x, y, z, t) \tilde{\rho}(z) dz = T_f^0 + T_f^1 \cdot \theta_1. \tag{2.18}$$

In the second equality above, the mass-averaged temperature T_f has been related to the first-baroclinic-mode potential temperature θ_1, by evaluating the integral in (2.18) and

using (2.17) and (2.13); the constants T_f^0 and T_f^1 arise from the integration.

This relationship will be useful later in moving between the variable θ_1, which is useful for the fluid dynamics, and the variable T_f, which is useful for radiative transfer. One other temperature quantity that will be of use later is the equivalent potential temperature,

$$\theta_{ef}(x,y,z,t) = \left(T_f^{tot}(x,y,z,t) + \frac{L_v}{c_p} r_f(x,y,z,t)\right)\left(\frac{p_0}{\tilde{p}(z)}\right)^{R_d/c_p}, \tag{2.19}$$

where the subscript f indicates that θ_{ef} is the value of θ_e within the free troposphere. In (2.19), we use a linearization of the exponential function that arises in the more comprehensive definition of $\theta_e \approx \theta \exp[L_v q_v/(c_p T)]$ [8], since the linearization allows simpler transformations between the variables θ_{ef}, T_f^{tot}, and r_f, and is reasonably accurate for present purposes. Of use later on is the value of θ_{ef} at the top of the boundary layer, by evaluating equation (2.19) at $z = 0$ one has

$$\begin{aligned}\theta_{ef}(x,y,0,t) &= \theta_f(x,y,0,t) + \left(\frac{L_v}{c_p} r_f(x,y,0,t)\right)\left(\frac{p_0}{\tilde{p}(0)}\right)^{R_d/c_p} \\ &= \theta_f^{ref} + \frac{L_v}{c_p} r_0.\end{aligned} \tag{2.20}$$

After defining $\theta_{ef}(x,y,0,t)$ as θ_{ef}^0, one can further rewrite as function of column water vapor quantity q_f in form of

$$\theta_{ef}^0(x,y,t) = \theta_f^{ref} + \frac{\tilde{L}_v^f}{c_p}\hat{Q}_0^{-1} q_f, \quad \text{with} \quad \tilde{L}_v^f = \frac{L_v \rho_o}{H_T \rho_f}. \tag{2.21}$$

2.1.3 Model variables of boundary layer

In the boundary layer, all variables are height-averaged and therefore independent of height, as illustrated in Fig. 1.4. The one exception is the vertical velocity, w_b, which is linear-in-height:

$$w_b(x,y,z,t) = -(z + h_b)\nabla \cdot \mathbf{u}_b(x,y,t), \tag{2.22}$$

where the horizontal divergence $\nabla \cdot \mathbf{u}_b$ appears here so that the velocity field satisfies the divergence-free constraint:

$$\nabla \cdot \mathbf{u}_b + \frac{\partial w_b}{\partial z} = 0. \tag{2.23}$$

The thermodynamic variables in the boundary layer are analogous to their counterparts in (2.13)–(2.19) from the free troposphere. Water will be partitioned into water vapor mixing ratio $r_{vb}(x, y, t)$ and liquid water mixing ratio $r_{lb}(x, y, t)$, and their sum, the total water mixing ratio $r_{tb}(x, y, t)$, where the subscript b denotes the boundary layer. The boundary-layer CWV and column total water are defined as

$$\begin{aligned} q_{vb}(x, y, t) &= \frac{\rho_b}{\rho_o} \int_{-h_b}^{0} r_{vb}(x, y, t)\, dz = h_b \frac{\rho_b}{\rho_o} r_{vb}(x, y, t), \\ q_{tb}(x, y, t) &= \frac{\rho_b}{\rho_o} \int_{-h_b}^{0} r_{tb}(x, y, t)\, dz = h_b \frac{\rho_b}{\rho_o} r_{tb}(x, y, t). \end{aligned} \tag{2.24}$$

The temperature T_b, potential temperature θ_b, and equivalent potential temperature θ_{eb} are related to each other via

$$T_b(x, y, t) = T_b^{ref} + \theta_b(x, y, t), \tag{2.25}$$

$$\theta_{eb}(x, y, t) = \left(T_b + \frac{L_v}{c_p} r_{vb} \right) \left(\frac{p_0}{p_b} \right)^{R_d/c_p} = T_b + \frac{\tilde{L}_v^b}{c_p} q_{vb}, \tag{2.26}$$

where $T_b^{ref} = 300$ K is a constant reference value of the atmospheric temperature near the ocean surface, where we have used $p_b \approx p_0$ in the θ_{eb} definition above, and where $\tilde{L}_v^b$ is a scaled latent heat in the boundary layer, with $\tilde{L}_v^b = L_v^b / h_b$ and $L_v^b = L_v(\rho_o/\rho_b)$. The definitions for the boundary layer in (2.24)–(2.26) are similar to (2.15)–(2.19) for the free troposphere.

2.1.4 Cloud indicators

The presence of clouds will be described by cloud indicator functions σ_f and σ_b for the free troposphere and boundary layer, respectively. To define the presence of a cloud, we

Table 2.2: Parameters of background states

parameters	value	unit	description
H_q	2000	m	Free troposphere moisture scale
Q_0	0.102	m	Background moisture stratification
Q_1	0.0183	m	Background barotropic vertical moisture advection
T_f^0	258.57	K	Background temperature in T_f
T_f^1	0.6905		Linear dependency of θ_1 in T_f
θ_f^{ref}	300	K	Reference temperature in free troposphere
$d\theta_{bg}/dz$	3	K km^{-1}	Vertical gradient of background potential temperature
$q_{b,sat,0}$	-262	mm	Background column water vapor in $q_{b,sat}$
$q_{b,sat,1}$	1	mm/K	Linear dependency of T_b in $q_{b,sat}$
$q_{f,sat,0}$	-235	mm	Background column water vapor in $q_{f,sat}$
$q_{f,sat,1}$	1	mm/K	Linear dependency of T_f in $q_{f,sat}$
F_o	0.0556	K/day	Forcing strength on ocean temperature

compare the moisture value q_f to a threshold value $q_{f,sat}$ and define

$$\sigma_f(x,y,t) = \mathcal{H}(q_f - q_{f,sat}), \qquad \sigma_b(x,y,t) = \mathcal{H}(q_{tb} - q_{b,sat}), \tag{2.27}$$

where $\mathcal{H}(q)$ is the Heaviside function, so that $\mathcal{H}(q) = 1$ if $q \geq 0$ and $\mathcal{H}(q) = 0$ if $q < 0$, and where similar expressions are used above for both σ_f and σ_b. The threshold or saturation values $q_{b,sat}$ and $q_{f,sat}$ are taken here to be linear functions of temperature:

$$q_{b,sat} = q_{b,sat,0} + q_{b,sat,1}T_b, \qquad q_{f,sat} = q_{f,sat,0} + q_{f,sat,1}T_f, \tag{2.28}$$

where $q_{b,sat,0}, q_{b,sat,1}, q_{f,sat,0}$, and $q_{f,sat,1}$ are constant parameters. The use of saturation values that are linear in temperature can be viewed as a linearization of the type of saturation mixing ratio that arises from the Clausius–Clapeyron equation of thermodynamics [54]. Alternatively, since these cloud indicators are defined on somewhat large scales, the saturation values could be viewed as empirical definitions that can be

defined based on observational data [55]. Note that the values of these parameters ($q_{b,sat,0}, q_{b,sat,1}, q_{f,sat,0}$, and $q_{f,sat,1}$) should tacitly depend on other parameters, such as boundary-layer height h_b and free troposphere height H_T, since q_{tb} and q_f are integrated over these heights, respectively. These cloud indicators will act as nonlinear switches that turn on or off certain physical processes, such as rainfall or cloud–radiation interactions, as described further below.

2.2 Evolution of free troposphere

Now that the variables have been described above in section 2.1, the dynamical equations of motion can be presented. The evolution equations for the free troposphere will be described first, followed by the evolution equations for the barotropic modes, the boundary layer and ocean.

2.2.1 Fluid dynamics core

The dynamics of the free troposphere is given by

$$\frac{\partial \mathbf{u}_1}{\partial t} - \alpha_1 \nabla \theta_1 = -\frac{1}{\tau_R}\mathbf{u}_1, \tag{2.29}$$

$$\frac{\partial \theta_1}{\partial t} - \alpha_2 \nabla \cdot \left(\mathbf{u}_1 - \sqrt{2}\mathbf{u}_0\right) = S_{\theta_1}, \tag{2.30}$$

for the first-baroclinic-mode velocity $\mathbf{u}_1$ and potential temperature θ_1, and

$$\frac{\partial q_f}{\partial t} + \nabla \cdot \left(Q_1 \mathbf{u}_1 - Q_0 \mathbf{u}_0\right) = S_{q_f} \tag{2.31}$$

for the free-tropospheric moisture. The barotropic velocity $\mathbf{u}_0$ will be described in the following section 2.3 due to its coupling with the boundary layer. In essence, (2.29)–(2.30) describes a shallow-water system for $\mathbf{u}_1(x, y, t)$ and $\theta_1(x, y, t)$, and a similar type of equation for q_f. Note that it is not the same as the traditional, single-layer shallow water equations, but it has connection to multi-mode or multi-layer shallow water equations,

as mentioned further below. The fluid flow will be driven by the heat source/sink S_{θ_1}, which is described further below and includes cloud latent heating that is interactive and evolving based on individual cloud clusters.

The left-hand side of (2.29)–(2.31) is the dynamical core, and it can be derived from the 3D fluid dynamics equations and the bulker water budget equation as follows [26, 28, 29, 33, 34, 44]. The starting point is the hydrostatic primitive equations

$$\frac{\partial u_f}{\partial t} + \frac{\partial p_f}{\partial x} = 0, \tag{2.32}$$

$$\frac{\partial v_f}{\partial t} + \frac{\partial p_f}{\partial y} = 0, \tag{2.33}$$

$$\frac{\partial p_f}{\partial z} = g\frac{\theta_f}{\theta_f^{ref}}, \tag{2.34}$$

$$\frac{\partial \theta_f}{\partial t} + w_f\frac{\partial \theta_{bg}}{\partial z} = 0, \tag{2.35}$$

$$\frac{\partial r_f}{\partial t} + w_f\frac{\partial r_{bg}}{\partial z} = 0. \tag{2.36}$$

Note that the hydrostatic assumption is a helpful assumption for deriving simplified equation sets although for grid spacings in the range of $O(1)$ to $O(10)$ km, it may not be the complete description of phenomena on the smallest model scales. Also note that nonlinear advection terms have been neglected, while advection of the background state $\theta_{bg}(z)$ is included, and advection of q has been linearized with respect to a background state $r_{bg}(z) = r_{00}\exp(-z/H_q)$. Nonlinear advection could possibly be included in the future [28, 29, 34], although a careful investigation is still needed for the interactions of nonlinear advection and stochasticity in the present type of framework, and numerical methods should therefore be chosen appropriately. Nonlinear advection could possibly be included in the future [28, 29, 34], although a careful investigation is still needed for the interactions of nonlinear advection and stochasticity in the present type of framework, and numerical methods should therefore be chosen appropriately. Some other climate

components that will be neglected in the idealized simulations here are spherical geometry of Earth, rotation, and the diurnal cycle, although these and other features could be added in the future.

To derive the shallow water system in (2.29)–(2.31), the vertical structures arise from a Sturm–Liouville problem and were described in (2.9)–(2.15). It then follows from (2.13) and from hydrostatic balance in (2.34) that the vertical structure of the (scaled) pressure is

$$p_f(x,y,z,t) = p_{bg}(z) + p_0(x,y,t) + p_1(x,y,t)\sqrt{2}\cos\frac{\pi z}{H_T}, \quad p_1 = -\frac{g}{\theta_f^{ref}}\frac{H_T}{\pi}\theta_1. \tag{2.37}$$

Then the evolution equations in (2.32)–(2.36) are projected onto the vertical structures from the Sturm–Liouville problem using the inner product

$$\langle f, g\rangle = \frac{1}{H_T}\int_0^{H_T} f(z)g(z)\,dz. \tag{2.38}$$

Since the vertical structure functions in (2.9)–(2.13) are sines and cosines as in a Fourier series, the projections and inner products are straightforward [28, 29, 33, 34, 44]. By projecting the momentum equations in (2.32)–(2.33) onto the basis function $\sqrt{2}\cos(\pi z/H_T)$, one has

$$\begin{aligned}
\partial_t\big\langle u_f(x,y,z,t), \sqrt{2}\cos\frac{\pi z}{H_T}\big\rangle + \partial_x\big\langle p_f(x,y,z,t), \sqrt{2}\cos\frac{\pi z}{H_T}\big\rangle = 0;\\
\partial_t\big\langle v_f(x,y,z,t), \sqrt{2}\cos\frac{\pi z}{H_T}\big\rangle + \partial_y\big\langle p_f(x,y,z,t), \sqrt{2}\cos\frac{\pi z}{H_T}\big\rangle = 0,
\end{aligned} \tag{2.39}$$

with vertical structures can be simplified through inner product as

$$\begin{aligned}
\partial_t \big\langle u_f(x,y,z,t), \sqrt{2}\cos\frac{\pi z}{H_T}\big\rangle &= \partial_t u_1(x,y,t),\\
\partial_t \big\langle v_f(x,y,z,t), \sqrt{2}\cos\frac{\pi z}{H_T}\big\rangle &= \partial_t v_1(x,y,t),\\
\partial_x \big\langle p_f(x,y,z,t), \sqrt{2}\cos\frac{\pi z}{H_T}\big\rangle &= \partial_x p_1(x,y,t),\\
\partial_y \big\langle p_f(x,y,z,t), \sqrt{2}\cos\frac{\pi z}{H_T}\big\rangle &= \partial_y p_1(x,y,t).
\end{aligned} \tag{2.40}$$

Together with relationship between pressure variable and potential temperature solved in (2.37), one arrives at the shallow-water momentum equations in (2.29) with $\alpha_1 = gH_T/(\pi\theta_f^{ref}) \approx 170$ m^2 s^{-2} K^{-1}. Similarly, by projecting the θ_f evolution equation in (2.35) onto the basis function $\sqrt{2}\sin(\pi z/H_T)$, one can calculate the inner product of vertical structures as

$$\begin{aligned}
\partial_t \big\langle \theta_f(x,y,z,t), \sqrt{2}\sin\frac{\pi z}{H_T}\big\rangle =& \partial_t \theta_1(x,y,t),\\
\big\langle w_f(x,y,z,t)\frac{\partial\theta_{bg}}{\partial z}, \sqrt{2}\sin\frac{\pi z}{H_T}\big\rangle =& w_0(x,y,t)\frac{d\theta_{bg}}{dz}\big\langle (H_T - z), \sqrt{2}\sin\frac{\pi z}{H_T}\big\rangle +\\
& w_1(x,y,t)\frac{d\theta_{bg}}{dz}\big\langle \sqrt{2}\sin\frac{\pi z}{H_T}, \sqrt{2}\sin\frac{\pi z}{H_T}\big\rangle,\\
=& w_0(x,y,t)\frac{d\theta_{bg}}{dz}\frac{\sqrt{2}H_T}{\pi} + w_1(x,y,t)\frac{d\theta_{bg}}{dz}.
\end{aligned} \tag{2.41}$$

Considering the fact vertical velocities can be expressed as divergence of horizontal component as shown in (2.12), one arrives at the shallow-water θ_1 equation in (2.30) with $\alpha_2 = (H_T/\pi)(d\theta_{bg}/dz) \approx 15$ K, where $d\theta_{bg}/dz = 3$ K km^{-1} is assumed constant.

Finally, for the moisture, we derive the fluids dynamics through the bulker water budget equation in the atmosphere, as similar equations of mixing ratio shown in [28, 29], given by

$$\frac{\partial r_f}{\partial t} + \nabla\cdot\big(r_f \boldsymbol{u}_f\big) + \frac{\partial(r_f w_f)}{\partial z} = S_{r_f}. \tag{2.42}$$

With the left hand side terms represent the vertical and horizontal transportation of water quantity through fluid system respectively. Considering that rewriting the bulker

equation in form of column water vapor quantity q_f will help our model in cleaner form. After applying vertical integral $\langle\cdot\rangle = \int_0^{H_T} dz$ to equation (2.42) one can get dynamics of CWV values as

$$\begin{aligned}
\langle \partial_t r_f \rangle &= \partial_t \langle r_f \rangle = \frac{\rho_f}{\rho_0 H_T} \partial_t q_f; \\
\big\langle \partial_z (r_f w_f) \big\rangle &= \frac{1}{H_T} r_f w_f \Big|_0^{H_T} = -r_0 \nabla \cdot \boldsymbol{u}_0 \\
&= -\frac{\rho_f}{\rho_0 H_T \hat{Q}_0} q_f \nabla \cdot \boldsymbol{u}_0. \\
\big\langle \nabla \cdot (r_f \boldsymbol{u}_f) \big\rangle &= \big\langle \nabla \cdot (r_f \boldsymbol{u}_0) \big\rangle + \big\langle \nabla \cdot (r_f \boldsymbol{u}_1 \sqrt{2} \cos \frac{\pi z}{H_T}) \big\rangle;
\end{aligned} \tag{2.43}$$

With the vertical integral of barotropic and baroclinic segments can be calculated as

$$\begin{aligned}
\big\langle \nabla \cdot (r_f \boldsymbol{u}_0) \big\rangle &= \nabla \cdot \big(\boldsymbol{u}_0 \langle r_f \rangle \big) = \frac{\rho_f}{\rho_0 H_T} \nabla \cdot (q_f \boldsymbol{u}_0); \\
\big\langle \nabla \cdot (r_f \boldsymbol{u}_1 \sqrt{2} \cos \frac{\pi z}{H_T}) \big\rangle &= \nabla \cdot \big(\phi(r_f) \boldsymbol{u}_1 \big),
\end{aligned} \tag{2.44}$$

with the vertical integral of mixing ratio being defined as $\phi(r_f) = \langle \sqrt{2} \cos \frac{\pi z}{H_T} r_f \rangle$. Noticing the vertical integral of background profile are already calculated as $\hat{Q}_0$ in equation (2.16), we can seek closures on the form $\phi(r_f) = \tilde{\alpha_1} \langle r_f \rangle$ with linear parameter $\tilde{\alpha}_1$ solved explicitly as function of layers' height via integrating by parts twice

$$\begin{aligned}
\tilde{\alpha}_1 &= \frac{\sqrt{2}}{H_T \hat{Q}_0} \int_0^{H_T} \exp(-z/H_q) \cos\big(\frac{\pi z}{H_T}\big) dz, \\
&= \frac{\sqrt{2} H_T^2}{H_T^2 + (\pi H_q)^2} \left[\frac{1 + \exp(-H_T/H_q)}{1 - \exp(-H_T/H_q)} \right].
\end{aligned} \tag{2.45}$$

Such parameter value is close to the estimated value in [28, 29], which under assumption of separation of variables $q_v = q + Q(z)$ instead of obtaining background profile as known exponential function. The corresponding parameter value in [29] were resolved by applying mean value theorem. Back to our vertical integral, one can further simplify equation (2.44) into

$$\big\langle \nabla \cdot (r_f \boldsymbol{u}_1 \sqrt{2} \cos \frac{\pi z}{H_T}) \big\rangle = \nabla \cdot \big(\tilde{\alpha}_1 \langle r_f \rangle \boldsymbol{u}_1 \big) = \frac{\rho_f \tilde{\alpha}_1}{\rho_0 H_T} \nabla \cdot (q_f \boldsymbol{u}_1). \tag{2.46}$$

By substituting all calculated vertical integrals (2.43)–(2.46) back into original bulker equation (2.42), also dividing out common factor and shuffling the sub-index of right-hand side forcing term. One has modified fluid dynamics of q_f as

$$\partial_t q_f + \big(1 - \hat{Q}_0^{-1}\big) q_f \nabla \cdot \mathbf{u}_0 + \tilde{\alpha}_1 q_f \nabla \cdot \mathbf{u}_1 + \big(\boldsymbol{u}_0 + \tilde{\alpha}_1 \boldsymbol{u}_1\big) \cdot \nabla q_f = S_{q_f}. \tag{2.47}$$

Finally by setting q_f values as constant $\hat{q}_f$ in equation (2.47), advection of q_f will be vanished and the linearized fluid dynamics of q_f just arrives at the form of equation shallow-water moisture equation in (2.31) with

$$Q_0 = -\big(1 - \hat{Q}_0^{-1}\big)\hat{q}_f, \qquad Q_1 = \tilde{\alpha}_1 \hat{q}_f. \tag{2.48}$$

Under the choice of $\hat{q}_f = 15$mm as typical constant value and explicit formula of $\tilde{\alpha}_1$ given in (2.45), the value of parameters Q_0 and Q_1 are listed in Table 2.2.

Note that the system in (2.29)–(2.31) is not the traditional, single-layer shallow water equations, but it can be viewed as one mode of multi-mode shallow water equations if additional vertical basis functions are considered [34]. Also, this connection with shallow water systems can be seen to arise because the primitive equations in (2.32)–(2.36) can be viewed as a multi-layer shallow water system; see Ref. [56], chapter 2, sections 18 and 19. This completes the derivation of the dynamical core on the left-hand side of the shallow-water-like system in (2.29)–(2.31).

2.2.2 Source and sink terms

On the right-hand side of (2.29)–(2.31) are the source/sink terms, which are interactive and evolving and defined in following subsection. In the momentum equation, the sink $-\mathbf{u}_1/\tau_R$ is a Rayleigh damping term. In the moisture equation, the source/sink S_{q_f} is

defined as

$$\begin{aligned} S_{q_f} = &- \frac{1}{\tau_q}\big[q_f - q_{f,sat}(T_f)\big]^+ + \big(\frac{\sigma_b}{\tau_{t,b}} + \frac{\sigma_b\sigma_f}{\tau_{t,f}}\big)\big[q_{tb} - q_f\frac{h_b\rho_b}{H_T\rho_f}\hat{Q}_0^{-1}\big]^+ \\ &+ b_{q_f}\nabla^2 q_f + D_f\dot{W}_f, \end{aligned} \tag{2.49}$$

and the four terms represent precipitation from deep-convective clouds, a moisture source from cloud-top mixing of boundary-layer clouds, eddy diffusion, and stochastic forcing, respectively. The precipitation term includes a superscript $^+$ that indicates a nonlinear switch, so that precipitation turns on only when q_f exceeds the threshold value $q_{f,sat}$, which is a function of temperature according to (2.18) and (2.28). The cloud-top mixing term is proportional to the difference between the water content in two layers and also forced to be positive under superscript $^+$ which means the water vapor can only be transported from boundary layer to free troposphere. A multi timescale involved both types of cloud indicator have been used here to describe three-stages of rainfall events in atmosphere. More specifically, the cloud indicator σ_b is a coefficient that turns on cloud-top mixing only when boundary-layer clouds are present, the segment with multiplied extra indicator σ_f and large rate of precipitation $\tau_{t,f}$ would allow a rapid moisture exchange process between layers when deep convection is performed. It is worth noting that the transform rate of moisture $\tau_{t,f}$ should be no faster than convection rate τ_q to maintain the water budget balance in free troposphere.

The eddy diffusion and stochastic forcing are a parameterization of turbulent advection–diffusion [57–60] and are similar to earlier models of spatiotemporal stochastic clouds. The value of, for instance, the eddy moisture diffusivity b_q may appear to be large when written in units of $\mathrm{m}^2\ \mathrm{s}^{-1}$, but it is more nearly $O(1)$ in magnitude when written in terms of equatorial synoptic scales, and its value was calibrated based on the power spectrum from observational data. The stochastic forcing $\dot{W}_f$ is a spatiotemporal white noise with mean zero and covariance $E[\dot{W}_f(x,y,t)\dot{W}_f(x',y',t')] = \delta(x-x')\delta(y-y')\delta(t-t')$, or a discretized version as described in the followed chapter 3. The values of the parameters

Table 2.3: Parameters of physical parameterizations

parameters	value	unit	description
τ_s	6	hours	Sensible heating time scale
τ_m	8	hours	Momentum entrainment time scale
τ_q	2	hours	Convection time scale
$\tau_{t,b}$	6	hours	Cloud top mixing time scale (drizzle)
$\tau_{t,f}$	24	hours	Cloud top mixing time scale (convection)
τ_e	6	days	Sea surface evaporation time scale
τ_R	75	days	Rayleigh drag time scale
C_d	0.025		Surface drag coefficient
U_p	2	m/s	Strength of turbulent coefficient
$\tilde{D}_b$	7.35	$\mathrm{m}/\sqrt{\mathrm{s}}$	Stochastic strength in q_{tb}
$\tilde{D}_f$	1.23	$\mathrm{m}/\sqrt{\mathrm{s}}$	Stochastic strength in q_f
b_v	6.25×10^2	m^2/s	Eddy viscosity
b_T	6.25×10^2	m^2/s	Eddy diffusivity in temperatures
b_q	6.25×10^5	m^2/s	Eddy diffusivity in moisture

from the source/sink terms are listed in Table 2.3.

Note that parameters of various types have been defined here, ranging from fundamental constants of nature such as c_p and L_v in Table 2.1 to parameters from physical parameterizations in Table 2.3. For the parameters that are related to physical parameterizations, such as cloud and precipitation processes, the values of the parameters are chosen to be in line with other studies and observational constraints (see, e.g., Refs. [22, 37] and references therein). Sensitivity studies have also been carried out for many of these parameters and presented in other studies (e.g., Refs. [22, 37]), and some additional sensitivity studies are presented below. While many parameters appear in the present idealized modeling framework, it is a relatively small number of parameters in comparison to comprehensive models such as LES, CRMs, and GCMs, since comprehensive models account for additional aspects, such as cloud microphysics and varying structures in the

vertical direction, which require additional parameters [2, 61].

As the last part of the shallow-water system, in the shallow-water equation for θ_1 in (2.30), the heat source/sink term is given by

$$S_{\theta_1} = \frac{1}{\tau_q} \cdot \frac{\tilde{L}_v^f}{c_p} \left[q_f - q_{f,sat}(T_f) \right]^+ + \frac{1}{C_f} F_{rad,f}, \tag{2.50}$$

where $C_f = c_p \rho_f H_T$ is a scaled version of the specific heat capacity. The first term is the cloud latent heating that is associated with precipitation in (2.31), and the coefficient $\tilde{L}_v^f / c_p$ is a latent heating factor, defined above in (2.21). Note that no stochastic forcing term was included for potential temperature in (2.50), for simplicity, whereas stochastic forcing was included for moisture in (2.49); additional stochastic forcing terms could be included, although they would increase the complexity of the model via the introduction of additional parameters and their calibration, and prior work has suggested that the minimal addition of stochasticity to only the moisture equation is sufficient for generating reasonable variability [44]. The second term is radiative heating/cooling; it is given by

$$\begin{aligned} F_{rad,f} = {} & S(1 - A_f \sigma_f) a_{sf} + S(1 - A_f \sigma_f)(1 - a_{sf}) a_{sf} A_b \sigma_b \\ & + a_{lf} a_{lb} \sigma T_b^4 + a_{lf}(1 - a_{lb}) \sigma T_o^4 - 2 a_{lf} \sigma T_f^4, \end{aligned} \tag{2.51}$$

and it is composed of five terms: absorption of downwelling solar radiation ($\propto S$), absorption of upwelling solar radiation that has reflected off of boundary layer clouds ($\propto S\sigma_b$), absorption of longwave radiation that was emitted by the boundary layer ($\propto \sigma T_b^4$) and ocean ($\propto \sigma T_o^4$), and emission of longwave radiation ($\propto \sigma T_f^4$), respectively. The radiative parameters are the solar constant S (averaged over a diurnal cycle); the Stefan–Boltzmann constant σ; the albedos A_f and A_b of deep convective and boundary layer clouds, respectively; the shortwave absorptivities a_{sf} and a_{sb} of the free troposphere and boundary layer, respectively; and the longwave absorptivities a_{lf} and a_{lb} of the free troposphere and boundary layer, respectively. The physical interpretation of the first solar radiation term, for instance, is that it represents a fraction of S that is absorbed by the free

troposphere, after a fraction $1-A_f\sigma_f$ is reflected at cloud-top by deep convective clouds in the free troposphere. The absorptivity a_{sf} defines the fraction of incoming radiation that is absorbed by the free troposphere. Further details of the radiation scheme are described in Ref. [37], which has been extended here in a straightforward way to include the effects of an evolving free troposphere and deep convective clouds.

Cloud–radiative feedbacks and water vapor feedback are included the radiation scheme in (2.51). As mentioned above, A_f and A_b are the albedos of deep convective and boundary layer clouds, respectively. Notice that these albedos always appear along with cloud indicators as $A_f\sigma_f$ and $A_b\sigma_b$, so that cloud–radiative feedback is turned on only when a cloud is present. Water vapor feedback is present in (2.51) through the absorptivities, a_{lf} and a_{lb}, which are defined as

$$\begin{aligned} a_{lf} &= a_{lf}^0 + a_{lf}^1\left[\frac{q_f}{q_{f,sat}} + \sigma_f\big(1-\frac{q_f}{q_{f,sat}}\big)\right], \\ a_{lb} &= a_{lb}^0 + a_{lb}^1\left[\frac{q_{vb}}{q_{b,sat}} + \sigma_b\big(1-\frac{q_{vb}}{q_{b,sat}}\big)\right]. \end{aligned} \tag{2.52}$$

These absorptivities will increase when the water vapor content increases, since water vapor is a greenhouse gas, and the effect is capped at a maximum value upon cloud formation. The parameter values for radiation are listed in Table 2.4.

Table 2.4: Radiation parameters.

parameter	value	unit	physical description
S	436	W m^{-2}	Solar flux at top of free troposphere
σ	5.67×10^{-8}	W m^{-2} K^{-4}	Stefan-Boltzmann constant
A_b	0.4		Albedo of shallow cloud
A_f	0.4		Albedo of deep cloud
a_{sb}	0.1		Shortwave absorptivity of boundary layer
a_{sf}	0.2		Shortwave absorptivity of free troposphere
a_{lb}^0	0.24		Longwave absorptivity of boundary layer (dry air)
a_{lb}^1	0.66		Longwave absorptivity of boundary layer (water vapor)
a_{lf}^0	0.2		Longwave absorptivity of free troposphere (dry air)
a_{lf}^1	0.7		Longwave absorptivity of free troposphere (water vapor)

2.3 Evolution of barotropic modes

The barotropic velocity $\boldsymbol{u}_0$ of the free troposphere is coupled to the atmospheric boundary layer velocity $\boldsymbol{u}_b$ as

$$\frac{\partial \mathbf{u}_b}{\partial t} + \frac{1}{\rho_{ref}} \nabla p_b = -\frac{\sigma_b}{h_b \tau_t} \big(\mathbf{u}_b - (\mathbf{u}_0 + \sqrt{2}\mathbf{u}_1) \big) - \frac{C_d U_p}{h_b} \mathbf{u}_b, \tag{2.53}$$

$$\frac{\partial \mathbf{u}_0}{\partial t} + \frac{1}{\rho_{ref}} \nabla p_0 = \frac{\sigma_b}{H_T \tau_t} \big(\mathbf{u}_b - (\mathbf{u}_0 + \sqrt{2}\mathbf{u}_1) \big), \tag{2.54}$$

$$h_b \nabla \cdot \mathbf{u}_b + H_T \nabla \cdot \mathbf{u}_0 = 0, \tag{2.55}$$

$$p_0 = p_b + \alpha_1 \rho_{ref} \left(\sqrt{2}\theta_1 + \frac{\pi}{2} \frac{h_b}{H_T} \theta_b \right), \tag{2.56}$$

where θ_b is the anomalous potential temperature in the boundary layer. In this coupling, divergence in the boundary layer is coupled with convergence in the barotropic mode in

the free troposphere, as defined in (2.55) and following earlier work [35, 45]. Also, as illustrated in Fig. 1.4, at the top of the boundary layer, the vertical velocity is continuous. The pressure relationship in (2.56) is also a continuity condition at the top of the boundary layer. Taken together, the dynamical core of (2.53)–(2.56) involves two pressure variables, p_b and p_0, although the pressure variables are related to each other, which leaves one pressure quantity to be associated with the single incompressibility condition in (2.55). Also, recall from section 2.1 that all boundary-layer variables are depth-averaged and therefore are functions of x, y, and t.

The source terms in (2.53)–(2.54) are related to mixing, drag, and dissipation. The surface drag in the boundary layer is $-(C_d U_p/h_b)\mathbf{u}_b$, where U_p is a measure of turbulent velocity strength and C_d is the non-dimensional surface drag coefficient. The source terms proportional to σ_b are a representation of momentum entrainment at the top of the boundary layer. They are functions of the difference in velocity between the boundary layer ($\mathbf{u}_b$) and the bottom of the free troposphere ($z = 0$), where the velocity $\mathbf{u}_f$ takes the value $\mathbf{u}_0 + \sqrt{2}\mathbf{u}_1$ and has contributions from both the baroclinic mode $\mathbf{u}_1$ and barotropic mode $\mathbf{u}_0$.

2.4 Evolution of boundary layer

For the thermodynamic variable evolution in the boundary layer, two quantities are used: total water mixing ratio q_{tb} and equivalent potential temperature θ_{eb}. The evolution of q_{tb} is given by

$$\begin{aligned}\frac{\partial q_{tb}}{\partial t} =& \frac{1}{\tau_e}\big(q_{b,sat}(T_o) - q_{tb}\big) - \big(\frac{\sigma_b}{\tau_{t,b}} + \frac{\sigma_b\sigma_f}{\tau_{t,f}}\big)\big[q_{tb} - q_f\frac{h_b\rho_b}{H_T\rho_f}\hat{Q}_0^{-1}\big]^+ \\ &+ b_{q_{tb}}\nabla^2 q_{tb} + D_b\dot{W}_b.\end{aligned} \tag{2.57}$$

Fig. 2.2 is a schematic illustration of the physical processes of the boundary layer. The first term on the right-hand side of (2.57) represents surface evaporation, and it is a source of moisture for the boundary layer. The second term involves multi timescales represents a

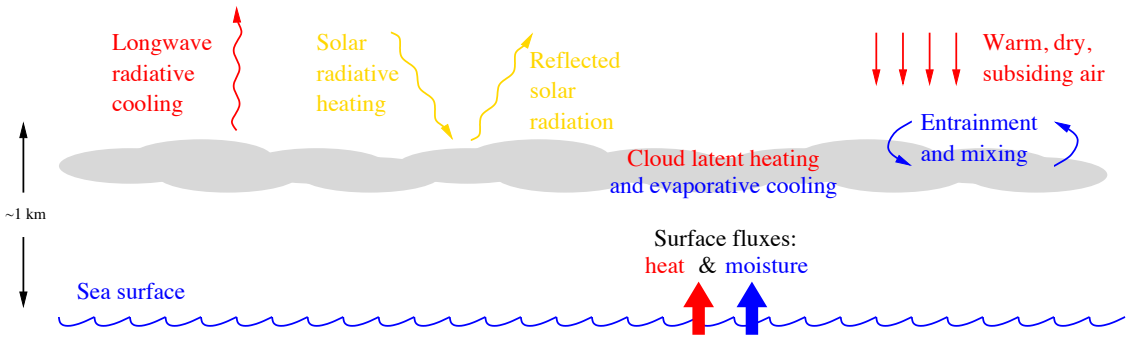

Figure 2.2: Schematic diagram of the physical processes related to the atmospheric boundary layer, including interactions with the ocean, free troposphere, and radiation. From [37]. Used with permission.

transfer of moisture from the boundary layer to the free troposphere via cloud-top mixing. It is forced to be a sink term and proportional to the difference in mixing ratio values between the boundary layer and free troposphere at the top of the boundary layer ($z = 0$). This mixing term also introduced an associated moistening term for the free troposphere in (2.49), illustrating that the water budget between boundary layer and free troposphere must be balanced. The last two terms on the right-hand side of (2.57) are a stochastic representation of turbulent advection–diffusion of moisture, as in Ref. [22] and also used for free tropospheric moisture in (2.31).

The evolution of the equivalent potential temperature in the boundary layer, θ_{eb}, is given by

$$\begin{aligned}\frac{\partial \theta_{eb}}{\partial t} = &- \frac{\tilde{L}_v^b}{c_p}\Big(\frac{\sigma_b}{\tau_{t,b}} + \frac{\sigma_b \sigma_f}{\tau_{t,f}}\Big)\big[q_{tb} - q_f \frac{h_b \rho_b}{H_T \rho_f}\hat{Q}_0^{-1}\big]^+ \\ &+ \frac{1}{\tau_s}\big(T_o - \theta_b\big) + \frac{1}{\tau_e}\cdot\frac{\tilde{L}_v^b}{c_p}\big(q_{b,sat}(T_o) - q_{tb}\big) + \frac{1}{C_b}F_{rad,b},\end{aligned} \tag{2.58}$$

where $C_b = c_p \rho_b h_b$ is a scaled version of the specific heat capacity. The first term on the right-hand side represents the latent heating induced by cloud-top mixing; it turns on only when a boundary layer cloud is present (i.e., when $\sigma_b = 1$), under the assumption that boundary layer cloud liquid water will evaporate upon mixing into the free troposphere. The second term is sensible heat transfer from the ocean, and it is proportional to the

difference between ocean temperature T_o and boundary-layer temperature or potential temperature θ_b. The third term is due to evaporation of water at the ocean surface, as also included in (2.57), and where $\tilde{L}_v^b = (L_v/h_b)(\rho_o/\rho_b)$ here is a scaled version of the latent heat of vaporization. The fourth term is due to radiation and is given by

$$\begin{aligned} F_{rad,b} =& S(1 - A_f\sigma_f)(1 - a_{sf})(1 - A_b\sigma_b)a_{sb} \\ &+ a_{lf}a_{lb}\sigma T_f^4 + a_{lb}\sigma T_o^4 - 2a_{lb}\sigma T_b^4, \end{aligned} \tag{2.59}$$

with terms that are similar to the free tropospheric radiation terms in (2.51). In particular, note that cloud feedbacks enter via $A_f\sigma_f$ and $A_b\sigma_b$, and water vapor feedback enters through the absorptivities a_{lf} and a_{lb}, which were defined in (2.52).

Note that the radiation scheme is formulated for simplicity in its definition, which is useful for ease of understanding the details of the model formulation. On the other hand, the simple formulation brings complications for comparisons with other models, which commonly use more comprehensive radiation schemes. For example, in climate-change experiments, it is common to change the concentration of carbon dioxide, which may be straightforward in a comprehensive radiation scheme, but which is less straightforward for a simplistic radiation scheme as used here, where the concentration of carbon dioxide is represented in a hitherto unspecified way through its influence on the absorptivity parameters a_{lb} and a_{lf}. By specifying these types of relationships between physically observed quantities and model parameters, one could pursue in the future a more quantitative comparison between the present idealized framework and more comprehensive model results.

2.5 Evolution of ocean temperature

Finally, the ocean temperature evolves according to

$$\frac{\partial T_o}{\partial t} = -\frac{1}{\tau_e} \cdot \frac{\tilde{L}_v^o}{c_o}\big(q_{b,sat}(T_o) - q_{tb}\big) - \frac{1}{\tau_s} \cdot \frac{C_b}{C_o}\big(T_o - T_b\big) + F_{merid,o} + \frac{1}{C_o}F_{rad,o}, \tag{2.60}$$

where $\tilde{L}_v^o = L_v/h_o$ is a scaled version of the latent heat of vaporization, and $C_o = c_o\rho_o h_o$ is a scaled version of the specific heat capacity. This type of model is sometimes called a slab ocean model since it describes the oceanic mixed-layer as a slab that interacts thermodynamically and radiatively with the atmosphere above it. A schematic diagram is shown in Fig. 2.2 to illustrate the physical processes of the ocean and the atmospheric boundary layer. The four terms on the right-hand side of (2.60) correspond to the physical processes of evaporation, sensible heat transfer, meridional heat transport, and radiation, respectively. Evaporation and sensible heat transfer typically cause a loss of heat in the ocean, whereas radiation is typically a heat source. The meridional heat transport is defined as

$$F_{merid,o} = F_o \sin\frac{2\pi x}{L_x}, \tag{2.61}$$

where L_x is the length of the domain in the x direction, and the value of parameter F_o is given in Table 2.2. Following earlier work [62], the prescribed meridional heat transport $F_{merid,o}$ is used to represent the effects of oceanic circulations in nature. The radiation term takes the form

$$\begin{aligned} F_{rad,o} =& S(1-a_{sf})(1-a_{sb})(1-A_f\sigma_f)(1-A_b\sigma_b) \\ &+ a_{lf}(1-a_{lb})\sigma T_f^4 + a_{lb}\sigma T_b^4 - \sigma T_o^4, \end{aligned} \tag{2.62}$$

and it is composed of four terms: absorption of solar radiation ($\propto S$), absorption of longwave radiation that was emitted by the free troposphere ($\propto \sigma T_f^4$) and boundary layer ($\propto \sigma T_b^4$), and emission of longwave radiation ($\propto \sigma T_o^4$), respectively. The physical interpretation of the solar radiation term, for instance, is that it represents a fraction of S that reaches the ocean surface, after a fraction $1 - A_f\sigma_f$ is reflected by deep convective clouds in the free troposphere, a fraction $1 - a_{sf}$ is absorbed by the free troposphere, a fraction $1 - A_b\sigma_b$ is reflected by boundary layer clouds, and a fraction $1 - a_{sb}$ is absorbed by the atmospheric boundary layer. Further details of the radiation scheme are described in Ref. [37], which has been extended here in a straightforward way to include the effects of an evolving free troposphere and deep convective clouds.

Chapter 3

Numerical method

The evolution equations of the model are (2.29)–(2.31), (2.53)–(2.56), (2.57), (2.58), and (2.60), and they are solved numerically using an operator splitting method. In the following chapter, some basic knowledge of numerical splitting and details of each single operators are described in section 3.1; the numerical simulation set-ups such as initial conditions together with parallel framework and computational cost are introduced in section 3.2.

3.1 Operator splitting method

By defining all model variables involved in operator splitting as time discretized form $\mathbf{U}^n = \mathbf{U}(t^n) = [T_o(t_n), \theta_{eb}(t_n), \theta_1, q_{tb}(t_n), q_f(t_n), \mathbf{u}_b(t_n), \mathbf{u}_0(t_n), \mathbf{u}_1(t_n)]^T$, with $t_n = n\Delta t$. Under the assumption that all model equations are linearized and can be splitted into three independent components, one can define three numerical operators to solve each components individually. We use $\mathcal{A}[\cdot], \mathcal{B}[\cdot]$ and $\mathcal{C}[\cdot]$ to define the numerical solvers which solving fluid dynamics, stochastic differential equations and physical ODEs (also updating cloud states) respectively. Then the time evolution of model equations can be described

in below simplified form,

$$\partial_t \mathbf{U}^n = \big(\mathcal{A} + \mathcal{B} + \mathcal{C}\big)[\mathbf{U}^n] \approx \mathcal{A}[\mathbf{U}^n] + \mathcal{B}[\mathbf{U}^n] + \mathcal{C}[\mathbf{U}^n]. \tag{3.1}$$

To illustrate the theoretical basement of splitting method and understand the $\approx$ sign in equation (3.1), one can solve above simplified process analytically as linear ordinary equation in single time step period. The time evolved solution updated by original model equations and operator splitting method can be represented as $\mathbf{U}^{n+1} = e^{(\mathcal{A}+\mathcal{B}+\mathcal{C})\Delta t}\mathbf{U}^n$ and $\hat{\mathbf{U}}^{n+1} = e^{\mathcal{A}\Delta t}e^{\mathcal{B}\Delta t}e^{\mathcal{C}\Delta t}$ respectively. By applying Taylor expansion as for time variable, one can obtain

$$\begin{aligned} e^{(\mathcal{A}+\mathcal{B}+\mathcal{C})\Delta t} &= 1 + (\mathcal{A} + \mathcal{B} + \mathcal{C})\Delta t + O(\Delta^2 t), \\ e^{\mathcal{A}\Delta t}e^{\mathcal{B}\Delta t}e^{\mathcal{C}\Delta t} &= (1 + \mathcal{A}\Delta t)(1 + \mathcal{B}\Delta t)(1 + \mathcal{C}\Delta t) + O(\Delta^2 t). \end{aligned} \tag{3.2}$$

The subtraction between two equations in (3.2) will indicate the first order of accuracy of operator splitting method, with $\mathbf{U}^{n+1} - \hat{\mathbf{U}}^{n+1} = O(\Delta t)$.

More specifically, for both operator $\mathcal{A}[\cdot]$ and $\mathcal{B}[\cdot]$ we will use spectral method to update fluid dynamical core and stochastic advection-diffusion equations in frequency space, followed with physical ODEs and cloud states updated through Forward Euler method in operator $\mathcal{C}[\cdot]$. The details of each numerical solvers will be introduced in below subsections respectively.

3.1.1 Fluid dynamics solver

The first operator is defined as fluid dynamics solver, which solves the fluid dynamical core of model equations, given by

$$\frac{\partial \mathbf{u}_1}{\partial t} - \alpha_1 \nabla \theta_1 = 0, \tag{3.3}$$

$$\frac{\partial \theta_1}{\partial t} - \alpha_2 \nabla \cdot \left(\mathbf{u}_1 - \sqrt{2}\mathbf{u}_0\right) = 0, \tag{3.4}$$

$$\frac{\partial q_f}{\partial t} + \nabla \cdot \left(Q_1 \mathbf{u}_1 - Q_0 \mathbf{u}_0\right) = 0, \tag{3.5}$$

$$\frac{\partial \mathbf{u}_b}{\partial t} + \frac{1}{\rho_{ref}} \nabla p_b = -\frac{C_d U_p}{h_b} \mathbf{u}_b, \tag{3.6}$$

$$\frac{\partial \mathbf{u}_0}{\partial t} + \frac{1}{\rho_{ref}} \nabla p_0 = 0, \tag{3.7}$$

$$h_b \nabla \cdot \mathbf{u}_b + H_T \nabla \cdot \mathbf{u}_0 = 0, \tag{3.8}$$

$$p_0 = p_b + \alpha_1 \rho_{ref} \left(\sqrt{2}\theta_1 + \frac{\pi}{2} \frac{h_b}{H_T} \theta_b\right), \tag{3.9}$$

with q_{tb}, θ_{eb}, and T_o held fixed. This fluid dynamical core is a linear, constant–coefficient system, and it can be solved semi-analytically using the Fourier transform. It is semi-analytical rather than analytical only because a numerical Fourier transform is used and because the eigenvalues and eigenvectors of the linear system are found numerically. The time integration can be solved analytically without the need for a numerical integration in time.

To eliminate the incompressibility condition in (3.8) and coupling pressure equation (3.9), a Helmholtz decomposition is applied to replace $\mathbf{u}_b$ and $\mathbf{u}_0$ by stream function ψ_i and velocity potential function ϕ_i, which can be obtained from the vorticiy and divergence of velocity fields. The relationships between vorticity and spatial divergence of 2D velocity

fields and corresponding stream function and potential function are given by

$$\begin{aligned}
\omega_0 &= \nabla \times \mathbf{u}_0 = -\nabla^2 \psi_0, \\
D_0 &= \nabla \cdot \mathbf{u}_0 = \nabla^2 \phi_0, \\
\omega_b &= \nabla \times \mathbf{u}_b = -\nabla^2 \psi_b, \\
D_b &= \nabla \cdot \mathbf{u}_b = \nabla^2 \phi_b.
\end{aligned} \tag{3.10}$$

Our goal is to update all the stream functions ψ_i and potential functions ϕ_i forward in time then re-build the updated velocity fields $\mathbf{u}_0$ and $\mathbf{u}_1$ under 2D Helmholtz decomposition,

$$\mathbf{u} = \nabla\phi - \nabla^{\perp}\psi = \left[\phi_x + \psi_y, \phi_y - \psi_x\right]^T. \tag{3.11}$$

The first step is to resolve pressure variables p_0 and p_b in a closure form of model variables thereby changing original fluid dynamical system into linear equations, which is the pre-condition of using spectral method.

One can apply curl operators to the momentum equations (3.6)–(3.7) to zero out the spatial derivatives of pressure variables,

$$\begin{aligned}
\frac{\partial \omega_0}{\partial t} &= -\frac{1}{\rho_{ref}} \nabla \times \nabla p_0 = 0, \\
\frac{\partial \omega_b}{\partial t} &= -\frac{1}{\rho_{ref}} \nabla \times \nabla p_b - \frac{C_d U_p}{h_b} \nabla \times \mathbf{u}_b = -\frac{C_d U_p}{h_b} \omega_b.
\end{aligned} \tag{3.12}$$

At the same time the spatial divergence operator can be also applied to (3.6)–(3.7) to obtain the divergence forms,

$$\begin{aligned}
\frac{\partial}{\partial t} H_T D_0 &= -\frac{H_T}{\rho_{ref}} \nabla^2 p_0, \\
\frac{\partial}{\partial t} h_b D_b &= -\frac{h_b}{\rho_{ref}} \nabla^2 p_b - C_d U_p \nabla \cdot \nabla \mathbf{u}_b \\
&= -\frac{h_b}{\rho_{ref}} \nabla^2 p_b - C_d U_p D_b.
\end{aligned} \tag{3.13}$$

Noticing that the incompressible flow condition (3.8) in divergence form can be written as

$h_b D_b + H_T D_0 = 0$. Together with above equation (3.13), one can arrive at the laplacian equation between pressure variables and potential function ϕ_b,

$$\Delta\left(\frac{H_T}{\rho_{ref}}p_0 + \frac{h_b}{\rho_{ref}}p_b + C_d U_p \phi_b\right) = 0. \tag{3.14}$$

To cancel out the laplacian operator Δ in (3.14), one can consider simplify this Poisson equation in Fourier space.

The Fourier series of given two dimensional function $f(x, y)$ in the box domain $[-L_x, L_x] \times [-L_y, L_y]$ can be represented by

$$f(x,y) = 4L_x L_y \sum_{k,l=-\infty}^{\infty} \hat{f}(k,l) \exp\left(ik\frac{\pi}{L_x}x + jl\frac{\pi}{L_y}y\right), \tag{3.15}$$

with the Fourier coefficient $\hat{f}(k, l)$ corresponding to specific Fourier mode (k, l) is calculated by

$$\hat{f}(k,l) = \frac{1}{4L_x L_y}\int_{-L_x}^{L_x}\int_{-L_y}^{L_y} f(x,y)\exp\big(-ik\frac{\pi}{L_x}x - jl\frac{\pi}{L_y}y\big)dydx. \tag{3.16}$$

We will further introduce the details of truncated Fourier series and discrete Fourier transformation (DFT) in the following section 3.2. For simplicity we just use $\mathcal{F}[f(x, y)] = \hat{f}(k, l)$ to represent 2D Fourier transformation process, and inverse Fourier transform $f(x, y) = \mathcal{F}^{-1}[\hat{f}(k, l)]$ can be illustrated by equation (3.15). More specifically, the properties of derivatives under Fourier transform are given by

$$\begin{aligned}
&\mathcal{F}[\partial_x f] = \hat{\partial}_x \hat{f} = ik\frac{\pi}{L_x}\hat{f},\\
&\mathcal{F}[\partial_x^n f] = \hat{\partial}_x^n \hat{f} = (\hat{\partial}_x)^n \hat{f} = \big(ik\frac{\pi}{L_x}\big)^n \hat{f}.\\
&\mathcal{F}[\partial_y f] = \hat{\partial}_y \hat{f} = jl\frac{\pi}{L_y}\hat{f},\\
&\mathcal{F}[\partial_y^n f] = \hat{\partial}_y^n \hat{f} = (\hat{\partial}_y)^n \hat{f} = \big(jl\frac{\pi}{L_y}\big)^n \hat{f}.
\end{aligned} \tag{3.17}$$

One can apply Fourier transforms to the equations in fluid dynamical core and update the Fourier coefficients of modes (k, l) individually in time by solving the linear system in

frequency space.

For given nonzero pair of wave numbers (k, l) (as for those special cases with zero Fourier mode or wave number been zeroed out we will introduce them as special case at the end of this subsection), by operating DFT to pressures' coupling condition (3.9) and equation (3.14), then dividing out the nonzero derivative operator $\hat{\Delta}$ one would have

$$\hat{p}_0 - \hat{p}_b = \alpha_1 \rho_{ref} \left(\sqrt{2}\hat{\theta}_1 + \frac{\pi}{2} \frac{h_b}{H_T} \hat{\theta}_b \right), \tag{3.18}$$

$$\frac{H_T}{\rho_{ref}} \hat{p}_0 + \frac{h_b}{\rho_{ref}} \hat{p}_b + C_d U_p \hat{\phi}_b = 0. \tag{3.19}$$

Under the assumption that θ_b was frozen at the beginning of fluid dynamics solver, which means during each time step $\frac{\pi}{2} \frac{h_b}{H_T} \hat{\theta}_b$ term will be regarded as fixed forcing in equation (3.18). From equations (3.18)–(3.19), one can resolve $\hat{p}_b$ and $\hat{p}_0$ as closed form of $\hat{\theta}_1$ and $\hat{\phi}_b$ as

$$\begin{aligned} \hat{p}_b &= \rho_{ref} \big[- C_d U_p \hat{\phi}_b - \sqrt{2}\alpha_1 H_T \hat{\theta}_1 - \frac{\pi}{2} \alpha_1 h_b \hat{\theta}_b \big] / \big(H_T + h_b \big), \\ \hat{p}_0 &= \rho_{ref} \big[- C_d U_p \hat{\phi}_b + \sqrt{2}\alpha_1 h_b \hat{\theta}_1 + \frac{\pi}{2} \alpha_1 \frac{h_b^2}{H_T} \hat{\theta}_b \big] / \big(H_T + h_b \big). \end{aligned} \tag{3.20}$$

Before substituting resolved $\hat{p}_b$ and $\hat{p}_0$ back into fluid dynamical equations, one need to use DFT set up the linear system in frequency space. The vorticity and divergence equations of velocity fields (3.12)–(3.13) can be re-write as equations of stream and potential functions ψ_i and ϕ_i, given by

$$\Delta \left(\frac{\partial \psi_0}{\partial t} \right) = 0, \tag{3.21}$$

$$\Delta \left(\frac{\partial \psi_b}{\partial t} - \frac{C_d U_p}{h_b} \psi_b \right) = 0, \tag{3.22}$$

$$\Delta \left(\frac{\partial H_T \phi_0}{\partial t} + \frac{H_T}{\rho_{ref}} p_0 \right) = 0, \tag{3.23}$$

$$\Delta \left(\frac{\partial h_b \phi_b}{\partial t} + \frac{h_b}{\rho_{ref}} p_b + C_d U_p \phi_b \right) = 0. \tag{3.24}$$

To obtain the linea system for all nonzero Fourier modes, after applying DFT and dividing

out the laplacian operator in (3.21)–(3.24), one has

$$\frac{\partial \hat{\psi}_0}{\partial t} = 0, \tag{3.25}$$

$$\frac{\partial \hat{\psi}_b}{\partial t} - \frac{C_d U_p}{h_b}\hat{\psi}_b = 0, \tag{3.26}$$

$$\frac{\partial H_T \hat{\phi}_0}{\partial t} + \frac{H_T}{\rho_{ref}}\hat{p}_0 = 0, \tag{3.27}$$

$$\frac{\partial h_b \hat{\phi}_b}{\partial t} + \frac{h_b}{\rho_{ref}}\hat{p}_b + C_d U_p \hat{\phi}_b = 0. \tag{3.28}$$

It's worth mentioning that the equations of Fourier transformed stream functions $\hat{\psi}_0$ and $\hat{\psi}_b$ are described as independent ODE form and can be solved analytically as function of t easily. For simplicity we will use super subscript n and $n+1$ to represent the function values at time t_n and $t_{n+1} = t_n + \Delta t$ respectively. Hence inside individual time step, we can evaluate $\hat{\psi}_0^{n+1}$ and $\hat{\psi}_b^{n+1}$ in frequency space from equations (3.25)–(3.26) by

$$\hat{\psi}_0^{n+1} = \hat{\psi}_0^n, \quad \hat{\psi}_b^{n+1} = \exp\left(\frac{C_d U_p}{h_b}\Delta t\right)\hat{\psi}_b^n. \tag{3.29}$$

To use 2D Helmholtz decomposition to recover velocity fields we still need to update potential function in time. Considering the special forms of $\hat{\phi}_i$ given in equations (3.27)–(3.28), one can denote

$$\begin{aligned} \hat{\phi}_+ &= h_b\hat{\phi}_b + H_T\hat{\phi}_0, \\ \hat{\phi}_- &= h_b\hat{\phi}_b - H_T\hat{\phi}_0, \\ \hat{\phi}_b &= (\hat{\phi}_+ + \hat{\phi}_-)/2h_b, \\ \hat{\phi}_0 &= (\hat{\phi}_+ - \hat{\phi}_-)/2H_T. \end{aligned} \tag{3.30}$$

Such change of variables will help us obtain and simplify the linear system in frequency space much easier, and we should notice $\hat{\phi}_\pm$ are defined in frequency space for nonzero Fourier modes $(k, l) \neq (0, 0)$ only. By substituting resolved pressure equations (3.20), the

equations of $\hat{\phi}_i$ can be illustrated as

$$\frac{\partial \hat{\phi}_+}{\partial t} = 0, \tag{3.31}$$

$$\begin{aligned}\frac{\partial \hat{\phi}_-}{\partial t} &= \frac{H_T}{\rho_{ref}}\hat{p}_0 - \frac{h_b}{\rho_{ref}}\hat{p}_b - C_d U_p \hat{\phi}_b \\ &= \frac{2\sqrt{2}\alpha_1 h_b H_T}{h_b + H_T}\hat{\theta}_1 + \frac{\pi \alpha_1 h_b^2}{h_b + H_T}\hat{\theta}_b - \frac{C_d U_p H_T}{h_b(h_b + H_T)}[\hat{\phi}_+ + \hat{\phi}_-].\end{aligned} \tag{3.32}$$

From equation (3.31) one can derive out the value of $\hat{\phi}$ is kept unchanged in frequency space. Which indicates that $\hat{\phi}_-$ is coupling with Fourier transformed model variables $\hat{\theta}_1$. Our next step is to modify original model equations into divergence form and constitute linear system in frequency space which can be solved semi-analytically in time.

To approach such linear system, by applying spatial divergence to $\mathbf{u}_1$'s equation and denote $w_1 = \nabla \cdot \mathbf{u}_1$, we can re-write equation (3.3) into divergence form as

$$\frac{\partial w_1}{\partial t} - \alpha_1 \Delta \theta_1 = 0. \tag{3.33}$$

At the same time based on the relationship between spatial divergence and potential function defined in (3.10), equation (3.4) can be represented as

$$\frac{\partial \theta_1}{\partial t} - \alpha_2 w_1 + \sqrt{2}\alpha_2 \Delta \phi_0 = 0. \tag{3.34}$$

The final step is just to employ Fourier transform to above divergence equations (3.33) and (3.34), together with change of variables defined in frequency space as in (3.30), the linear system contained with $\hat{w}_1$, $\hat{\theta}_1$ and $\hat{\phi}_-$ is given in closure form as

$$\frac{\partial \hat{w}_1}{\partial t} - \alpha_1 \hat{\Delta} \hat{\theta}_1 = 0, \tag{3.35}$$

$$\frac{\partial \hat{\theta}_1}{\partial t} - \alpha_2 \hat{w}_1 - \frac{\alpha_2}{\sqrt{2}H_T}\hat{\Delta}\hat{\phi}_- = -\frac{\alpha_2}{\sqrt{2}H_T}\hat{\Delta}\hat{\phi}_+, \tag{3.36}$$

$$\frac{\partial \hat{\phi}_-}{\partial t} + \frac{C_d U_p H_T}{h_b(h_b + H_T)}\hat{\phi}_- - \frac{2\sqrt{2}\alpha_1 h_b H_T}{h_b + H_T}\hat{\theta}_1 = \frac{\pi \alpha_1 h_b^2}{h_b + H_T}\hat{\theta}_b - \frac{C_d U_p H_T}{h_b(h_b + H_T)}\hat{\phi}_+. \tag{3.37}$$

Here $\hat{\Delta}$ means the laplacian operator under discrete Fourier transform, which can be expressed as function of specific wave number (k,l) as $\hat{\Delta}(k,l) = -\left(\frac{\pi}{L_x}\right)k^2 - \left(\frac{\pi}{L_y}\right)l^2$. The negative sign comes from square of unit image number i^2. Under the assumption that $\hat{\theta}_b$ and $\hat{\phi}_+$ are time-independent, the right-hand side of equations (3.35)–(3.37) can be regarded as fixed forcing term. Denoting $\hat{\mathbf{U}} = [\hat{w}_1, \hat{\theta}_1, \hat{\phi}_-]^T$, finally we obtained 3×3 linear system of $\hat{\mathbf{U}}$ in frequency space, one can re-write equations (3.35)–(3.37) in matrix form as

$$\partial_t \hat{\mathbf{U}} + \mathbf{A}_{k,l}\hat{\mathbf{U}} = \mathbf{F}_{k,l}. \tag{3.38}$$

With given nonzero wave number (k,l), the coefficients matrix $\mathbf{A}$ and loading vector $\mathbf{F}$ are given by

$$\mathbf{A}_{k,l} = \begin{bmatrix} 0 & \alpha_1\left(\frac{\pi^2}{L_x^2}k^2 + \frac{\pi^2}{L_y^2}l^2\right) & 0 \\ -\alpha_2 & 0 & \frac{\alpha_2}{\sqrt{2}H_T}\left(\frac{\pi^2}{L_x^2}k^2 + \frac{\pi^2}{L_y^2}l^2\right) \\ 0 & -\frac{2\sqrt{2}\alpha_1 h_b H_T}{h_b + H_T} & \frac{C_d U_p H_T}{(H_T + h_b)h_b} \end{bmatrix}, \tag{3.39}$$

$$\mathbf{F}_{k,l} = \begin{bmatrix} 0 & -\frac{\alpha_2}{\sqrt{2}H_T}\left(\frac{\pi^2}{L_x^2}k^2 + \frac{\pi^2}{L_y^2}l^2\right)\hat{\phi}_+ & \frac{\pi\alpha_1 h_b^2}{h_b + H_T}\hat{\theta}_b - \frac{C_d U_p H_T}{h_b(h_b + H_T)}\hat{\phi}_+ \end{bmatrix}^T. \tag{3.40}$$

Which is 3×3 linear system can be solved semi-analytically, under the condition that we have accurate eigan pairs of each coefficient matrix $\mathbf{A}[k,l]$ it can further solved analytically in time.

We will illustrate the method of using eigan value decomposition and change of variables to solve linear system $\partial_t \hat{\mathbf{U}} + \mathbf{A}[k,l]\hat{\mathbf{U}} = \mathbf{F}[k,l]$, for simplicity we just use $\mathbf{A}$ and $\mathbf{F}$ to represent the coefficient matrix and loading vector below. Considering the eigan pairs of $\mathbf{A}$ is given by $[\mathbf{V}, \mathbf{D}]^T$, which $\mathbf{D}$ is the diagonal matrix of all eigan values and $\mathbf{V}$ is the corresponding eigan vector matrix. We first apply change of variable $\mathbf{U} = \mathbf{VW}$, so that $\mathbf{W} = \mathbf{V}^{-1}\mathbf{U}$. Hence the original linear system of $\mathbf{U}$ can be transformed into

$$\partial_t \mathbf{U} + \mathbf{AU} = \mathbf{F} \Rightarrow \partial_t \mathbf{VW} + \mathbf{AVW} = \mathbf{F}. \tag{3.41}$$

By multiplying matrix $\mathbf{V}^{-1}$ on both sides one can further re-write it into diagonalized linear system

$$\begin{aligned} \mathbf{V}^{-1}\partial_t \mathbf{V}\mathbf{W} + \mathbf{V}^{-1}\mathbf{V}\mathbf{D}\mathbf{W} &= \mathbf{V}^{-1}\mathbf{F}, \\ \partial_t \mathbf{W} + \mathbf{D}\mathbf{W} &= \mathbf{V}^{-1}\mathbf{F}. \end{aligned} \tag{3.42}$$

With the scalar equation for each fixed coordinator i is given as $\partial_t W_i + D_{ii} W_i = \left(\mathbf{V}^{-1}\mathbf{F}\right)_i$. Such scalar equation can be solved analytically by using integral factor, as function of time t, and one can continue to rewrite the solution in matrix form as

$$\begin{aligned} \partial_t\left(e^{D_{ii}t} W_i\right) &= e^{D_{ii}t}\left(\mathbf{V}^{-1}\mathbf{F}\right)_i, \\ e^{D_{ii}t} W_i(t) - W_i(0) &= \left(\mathbf{V}^{-1}\mathbf{F}\right)_i \int_0^t e^{D_{ii}s} ds, \\ W_i(t) &= e^{-D_{ii}t} \int_0^t e^{D_{ii}s} ds \cdot \left(\mathbf{V}^{-1}\mathbf{F}\right)_i + e^{-D_{ii}t} W_i^0, \\ W_i(t) &= \frac{1 - e^{-D_{ii}t}}{D_{ii}} \left(\mathbf{V}^{-1}\mathbf{F}\right)_i + e^{-D_{ii}t} W_i(0), \\ \mathbf{W}(t) &= \mathbf{\Sigma}_1(t)\mathbf{V}^{-1}\hat{\mathbf{F}} + \mathbf{\Sigma}_2(t)\mathbf{W}(0). \end{aligned} \tag{3.43}$$

With $\mathbf{\Sigma}_1(t) = \mathrm{diag}\left(\dfrac{1 - e^{-D_{ii}t}}{D_{ii}}\right)$ and $\mathbf{\Sigma}_2(t) = \mathrm{diag}(e^{-D_{ii}t})$ are time-dependent matrices. Inside each time step the initial condition is given by $\mathbf{U}(t) = \mathbf{U}^n$ then the semi-analytically solution of $\mathbf{U}(t + \Delta t) = \mathbf{U}^{n+1}$ is given by

$$\mathbf{U}^{n+1} = \mathbf{V}\mathbf{W}(\Delta t) = \mathbf{V}\mathbf{\Sigma}_1(\Delta t)\mathbf{V}^{-1}\mathbf{F} + \mathbf{V}\mathbf{\Sigma}_2(\Delta t)\mathbf{V}^{-1}\mathbf{U}^n. \tag{3.44}$$

Noticing such analytically solution exists if and only if the coefficient matrix $\mathbf{A}$ is full rank, which is the main reason we force the wave number must be nonzero.

Hence for all Fourier modes with nonzero wave number (k, l), we can update spectrum variables $\hat{\mathbf{U}}$ forward in time to obtain $[\hat{w}_1^{n+1}, \hat{\theta}_1^{n+1}, \hat{\phi}_-^{n+1}]^T$. To further evolve model variables in time, we need to employ inverse Fourier transformation, which needs information of all Fourier modes, including special Fourier modes such as zero mode and some modes with highest wave number, we will give more details about zeroing out such

highest wave number in following subsection 3.2. To resolve the fluid dynamics as for zero mode, one can apply Fourier transform to equations (3.3)–(3.9) straightforwardly, and under the condition both wave number $k = l = 0$, all spatial derivatives will be vanished, thus

$$\begin{aligned} \frac{\partial \hat{\mathbf{u}}_1(0,0)}{\partial t} &= \frac{\partial \hat{\theta}_1(0,0)}{\partial t} = \frac{\partial \hat{\mathbf{u}}_0(0,0)}{\partial t} = 0, \\ \frac{\partial \hat{\mathbf{u}}_b(0,0)}{\partial t} &= -\frac{C_d U_p}{h_b} \hat{\mathbf{u}}_b(0,0). \end{aligned} \tag{3.45}$$

One can find the zero mode of $\hat{\mathbf{u}}_0$, $\hat{\mathbf{u}}_1$ and $\hat{\theta}_1$ are independent of time and $\hat{\mathbf{u}}_b(0,0)$ can be solved analytically from simple ODE.

Right now we are ready to recover model variables back to physical space. The temperature variable $\hat{\theta}_1^{\,n+1}$ is solved by the linear system (3.38) directly. The baroclinic mode $\hat{\mathbf{u}}_1^{n+1} = [\hat{u}_1^{n+1}, \hat{v}^{n+1}]^T$ can be resolved from updated divergence and vorticity functions

$$\hat{\partial x}\hat{u}_1^{n+1} + \hat{\partial y}\hat{v}_1^{n+1} = \hat{w}_1^{n+1}, \tag{3.46}$$

$$\hat{\partial y}\hat{u}_1^{n+1} - \hat{\partial y}\hat{v}_1^{n+1} = \hat{\partial y}\hat{u}_1^{n} - \hat{\partial y}\hat{v}_1^{n} \tag{3.47}$$

Here equation (3.47) can be derived through applying curl operator then take discrete Fourier transform to equation (3.3). With $\hat{w}_1^{n+1}$ being updated from linear system (3.38), one can solve equations (3.46)–(3.47) in closure form as

$$\begin{aligned} \hat{u}_1^{n+1} &= \big(\hat{\partial x}\hat{w}_1^{n+1} + \hat{\partial y}^{\,2}\hat{u}_1^{n} - \hat{\partial x}\hat{\partial y}\hat{v}_1^{n}\big)/\big(\hat{\partial x}^{\,2} + \hat{\partial y}^{\,2}\big), \\ \hat{v}_1^{n+1} &= \big(\hat{\partial y}\hat{w}_1^{n+1} + \hat{\partial x}^{\,2}\hat{v}_1^{n} - \hat{\partial x}\hat{\partial y}\hat{u}_1^{n}\big)/\big(\hat{\partial x}^{\,2} + \hat{\partial y}^{\,2}\big). \end{aligned} \tag{3.48}$$

To update two barotropic modes $\hat{\mathbf{u}}_0^{n+1}$ and $\hat{\mathbf{u}}_b^{n+1}$, as described in (3.11) 2D Helmholtz decomposition will be employed. With time evolution of stream functions $\hat{\psi}_0^{n+1}$ and $\hat{\psi}_b^{n+1}$ are given in (3.29). Moreover, the potential functions $\hat{\phi}_0^{n+1}$ and $\hat{\phi}_b^{n+1}$ can be resolved from change of variables as in (3.30), with $\hat{\phi}_+^{n+1}$ and $\hat{\phi}_-^{n+1}$ are updated by equation (3.31) and

linear system (3.38) respectively. Overall one has

$$\hat{\mathbf{u}}_0^{n+1} = [\hat{\partial x}\hat{\phi}_0^{n+1} + \hat{\partial y}\hat{\psi}_0^{n+1}, \hat{\partial y}\hat{\phi}_0^{n+1} - \hat{\partial x}\hat{\psi}_0^{n+1}]^T, \tag{3.49}$$

$$\hat{\mathbf{u}}_b^{n+1} = [\hat{\partial x}\hat{\phi}_b^{n+1} + \hat{\partial y}\hat{\psi}_b^{n+1}, \hat{\partial y}\hat{\phi}_b^{n+1} - \hat{\partial x}\hat{\psi}_b^{n+1}]^T, \tag{3.50}$$

The final step will be apply inverse Fourier transform $\mathcal{F}^{-1}$ to above updated Fourier modes and obtain time-evolved model variables in physical space as $\mathbf{u}_i^{n+1} = \mathcal{F}^{-1}[\hat{\mathbf{u}}_i^{n+1}], \theta_1^{n+1} = \mathcal{F}^{-1}[\hat{\theta}_1^{n+1}]$.

As the last part of fluid dynamics solver, the evolution of equation (3.5) can be operated individually through spectrum method. More specifically, one can calculate the numerical estimation of spatial divergence in frequency space and update $\hat{q}_f$ in time direction via forward Euler method,

$$\hat{q}_f^{n+1} = \hat{q}_f^n + \Delta t\big(Q_0\hat{\nabla}\cdot\hat{\mathbf{u}}_0 - Q_1\hat{\nabla}\cdot\hat{\mathbf{u}}_1\big). \tag{3.51}$$

At the end solve q_f in physical space via inverse Fourier transform $q_f^{n+1} = \mathcal{F}^{-1}[\hat{q}_f^{n+1}]$.

3.1.2 Stochastic equations solver

The second part of the splitting is the stochastic representation of turbulent advection–diffusion from (2.31) and (2.57),

$$\frac{\partial q_f}{\partial t} = b_q\nabla^2 q_f + D_f\dot{W}_f, \tag{3.52}$$

$$\frac{\partial q_{tb}}{\partial t} = b_q\nabla^2 q_{tb} + D_b\dot{W}_b, \tag{3.53}$$

which evolves q_f and q_{tb} while holding all other variables fixed. For this part of the evolution, a Fourier transform is used, and (3.52)–(3.53) becomes a system of independent Ornstein–Uhlenbeck processes that can be solved analytically [21, 63]. Basically above two equations have the same form but with different sub indices to represent the column water vapor quantities in atmospheric boundary layer and free troposphere respectively.

For simplicity in this subsection we will drop the sub indices and use q to describe the moisture content, D to represent the stochastic force strength and W means white noise, the standard stochastic heat equation is given by

$$\partial_t q = b\nabla^2 q + D\dot{W}. \tag{3.54}$$

As being formulated in [21], one can apply discrete Fourier transform to (3.54) hence in frequency space the equation will be decoupled for each Fourier modes individually. For given wave number (k, l), the equation of $\hat{q}_{k,l}(t)$ can be illustrated as

$$\partial_t \hat{q}_{k,l} = -c_{k,l}\hat{q}_{k,l} + D\hat{\dot{W}}_{k,l}, \tag{3.55}$$

where $c_{k,l}$ is defined as diffusion coefficient depends on wave number (k, l) and can be calculated from the Fourier transformed laplacian operator as

$$c_{k,l} = \hat{\Delta}_{k,l} = b\left(\frac{\pi^2}{L_x^2}k^2 + \frac{\pi^2}{L_y^2}l^2\right). \tag{3.56}$$

The second term on right-hand side $\hat{\dot{W}}_{k,l}(t)$ is obtained by the discrete Fourier transform of $\hat{W}_{i,j}$, which are independent Gaussian random variable that follows symmetric property of Fourier coefficients. Under such property, all the Fourier modes (k_1, l_1) and (k_2, l_2) with $k_1 + k_2 = l_1 + l_2 = 0$ will have corresponding coefficients forced to be complex conjugate, so that the reality constrain will be satisfied automatically. Hence equation (3.55) defines a complex Ornstein-Uhlenbeck process, which can be solved semi-analytically by integrating for time variable t. For single time step, the initial time is given by t and ending time equals $t + \Delta t$, the solution of (3.55) in the frequency space can be written as

$$\hat{q}_{k,l}(t + \Delta t) = e^{-c_{k,l}\Delta t}\hat{q}_{k,l}(t) + D\int_t^{t+\Delta t} e^{-c_{k,l}(t+\Delta t-s)}d\hat{W}_{k,l}(s), \tag{3.57}$$

Noticing that our diffusion coefficients $c_{k,l}$ defined in (3.56) is forced to be non-negative,

thus the first term in time integral (3.57) is regard as exponential decay of initial Fourier coefficients. The second term is time integral of white noise, which can be illustrated as Riemann sum of independent Gaussian random variables, based on the property that Brownian motion has independent Gaussian increasement. This integral has zero mean value and variance is solved analytically in [21], given by

$$\mathrm{Var}_{k,l} = \mathrm{Var}\left[D\int_t^{t+\Delta t} e^{-c_{k,l}(t+\Delta t-s)}d\hat{W}_{k,l}(s)\right] = \frac{D^2}{2c_{k,l}}(1-e^{-2c_{k,l}\Delta t}). \tag{3.58}$$

It's worth mentioning that the diffusion coefficient $c_{k,l}$ is at the position of denominator in (3.58), thus the zero Fourier mode $c_{0,0}=0$ would lead to singularity in analytical formula. Hence for this special Fourier mode with zero wave numbers, we just plug $k=l=0$ into (3.57) to obtain the stochastic integral as $D\int_t^{t+\Delta t} e^{-c_{0,0}\Delta t}d\hat{W}_{0,0}(s) = D\int_t^{t+\Delta t} d\hat{W}(s) = D\hat{W}(\Delta t)$, which is standard Brownian motion with variance equals $D^2\Delta t$.

Finally one obtain the updated Fourier coefficients $\hat{q}_{k,l}^{n+1} = \hat{q}_{k,l}(t+\Delta t)$ for each modes which equals exponential decay component together with Gaussian random variable with zero mean and variance $\mathrm{Var}_{k,l}$, leading to $q^{n+1} = \mathcal{F}^{-1}[\hat{q}_{k,l}^{n+1}]$. There are multiple methods to solve stochastic equation (3.54), including spectral method which generates white noise in physical space then apply Fourier transform to such random variable, and just use finite difference method to evaluate the diffusion operator and white noise $\hat{W}$ directly. More specifically, the spatiotemporal white noise terms, of the form $D\dot{W}(x,y,t)$ with strength parameter D, are included in (3.52)–(3.53). For a continuum model, it is well-known that the stochastic heat equation with spatiotemporal white noise forcing will not generate an evolution with finite variance in two spatial dimensions; as a result, to obtain an evolution with finite variance, $\dot{W}(x,y,t)$ must be regularized or discretized. Here we discretize $D\dot{W}(x,y,t)$ in the natural way as $\tilde{D}\dot{W}_{ij}(t)$, which is an independent white noise at each grid point (x_i,y_j), and where $\tilde{D} = D/(\Delta x\Delta y)^{1/2}$. By scaling $\tilde{D}$ with factors of $\Delta x^{1/2}$ and $\Delta y^{1/2}$, the covariance of $\tilde{D}\dot{W}_{ij}(t)$ will approximate the covariance of $D\dot{W}(x,y,t)$. While we generates the white noise in frequency space with variance solved

theoretically as (3.58) avoids the process of discretizing random variable $W(x, y, t)$, which is one of the advantage of stochastic solver.

To summarize, our numerical splitting method contains three independent numerical solver $\mathcal{A}[\cdot]$, $\mathcal{B}[\cdot]$ and $\mathcal{C}[\cdot]$. Which $\mathcal{A}[\cdot]$ is fluid dynamic solver that updating model variables at beginning time point t as

$$\begin{aligned}
&\mathbf{u}_b^1(t+\Delta t), \mathbf{u}_0^1(t+\Delta t), \mathbf{u}_1^1(t+\Delta t) = \mathcal{A}[\mathbf{u}_b(t), \mathbf{u}_0(t), \mathbf{u}_1(t)], \\
&\theta_1^1(t+\Delta t), q_f^1(t+\Delta t) = \mathcal{A}[\theta_1^1(t+\Delta t), q_f(t)], \\
&T_o^1(t+\Delta t), \theta_{eb}^1(t+\Delta t), q_{tb}^1(t+\Delta t) = T_o(t), \theta_{eb}(t), q_{tb}(t).
\end{aligned} \tag{3.59}$$

Where $\mathcal{B}[\cdot]$ is stochastic equation solver that adding randomness to column water vapor variables as

$$\begin{aligned}
&q_{tb}^2(t+\Delta t), q_f^2(t+\Delta t) = \mathcal{B}[q_{tb}^1(t+\Delta t), q_f^1(t+\Delta t)], \\
&T_o^2(t+\Delta t), \theta_{eb}^2(t+\Delta t), \theta_1^2(t+\Delta t) = T_o^1(t+\Delta t), \theta_{eb}^1(t+\Delta t), \theta_1^1(t+\Delta t), \\
&\mathbf{u}_b^2(t+\Delta t), \mathbf{u}_0^2(t+\Delta t), \mathbf{u}_1^2(t+\Delta t) = \mathbf{u}_b^1(t+\Delta t), \mathbf{u}_0^1(t+\Delta t), \mathbf{u}_1^1(t+\Delta t).
\end{aligned} \tag{3.60}$$

At the end $\mathcal{C}[\cdot]$ will evaluate all source and sink terms at the right-hand side of model equations, then discretizing in time by using Forward Euler method, and obtaining all model variables at ending time point $t + \Delta t$ as

$$\begin{aligned}
&q_{tb}(t+\Delta t), q_f(t+\Delta t) = \mathcal{C}[q_{tb}^2(t+\Delta t), q_f^2(t+\Delta t)], \\
&T_o(t+\Delta t), \theta_{eb}(t+\Delta t), \theta_1(t+\Delta t) = \mathcal{C}[T_o^2(t+\Delta t), \theta_{eb}^2(t+\Delta t), \theta_1^2(t+\Delta t)], \\
&\mathbf{u}_b(t+\Delta t), \mathbf{u}_0(t+\Delta t), \mathbf{u}_1(t+\Delta t) = \mathcal{C}[\mathbf{u}_b^2(t+\Delta t), \mathbf{u}_0^2(t+\Delta t), \mathbf{u}_1^2(t+\Delta t)].
\end{aligned} \tag{3.61}$$

After concluding all model variables then we will update cloud status σ_b, σ_c by Heaviside indicator functions defined as (2.27) and saturation values $q_{b,sat}, q_{f,sat}$ that defined in (2.28). One can use $t + \Delta t$ as new start time point and move forward to next time step. More details of numerical set such as initial conditions, time scale constrains and computational set up will be given in following subsection 3.2.

3.2 Simulation set up and computational cost

The domain size here is 10,000 km in the zonal (x) direction and 1000 km in the meridional (y) direction. These choices allow the model to represent one branch of the global Walker circulation, such as the circulation cell over the Pacific ocean, and also to represent mesoscale convective systems as stochastic cloud clusters. Doubly periodic boundary conditions are used in the x and y directions. Alternatively, another reasonable choice for boundary conditions could be a channel domain with boundaries at the north and south edges of the domain. One disadvantage of channel boundaries is that the simulation features may be influenced by the boundaries, and the region near the boundary may need to be neglected when calculating statistics. For this reason, periodic boundary conditions can be desirable instead, since the statistics are homogeneous in space and are not influenced by any boundaries.

The grid spacing is $\Delta x = \Delta y = 5$ km, which is chosen to be the same as in earlier studies with spatiotemporal stochastic models for clouds [21, 22]. The time step is $\Delta t = 1$ minute, and it is chosen to resolve all time scales involved in the system, including wave oscillation time scales and physical parameterization time scales. As a brief summary of the analysis of all such time scales, it is the wave oscillations that are the limiting factor, or possibly eddy diffusion if the eddy diffusivity is large. The wave propagation speed of the first baroclinic mode $(\mathbf{u}_1, \theta_1)$ is varied with different wave numbers. We attached the plot of wave speed $c_{wave}(k)$ along with wave number k in Fig. 3.1, with the first mode obtains maximum of wave speed equals roughly max $c_{wave} \approx 50$ m/s. So that the time step should be smaller than roughly $\Delta x / c_{wave} \approx 100$ s. With such a time step, to simulate 10 years of weather and climate evolution will require roughly $5 * 10^6$ time steps.

The initial conditions are chosen to be near a climate equilibrium state, in order to help reach a statistical equilibrium with a minimal amount of transient spin-up time. The initial guess for a climate equilibrium state is based on an earlier version of the model [37] which was spatially uniform. In particular, the spatially uniform component

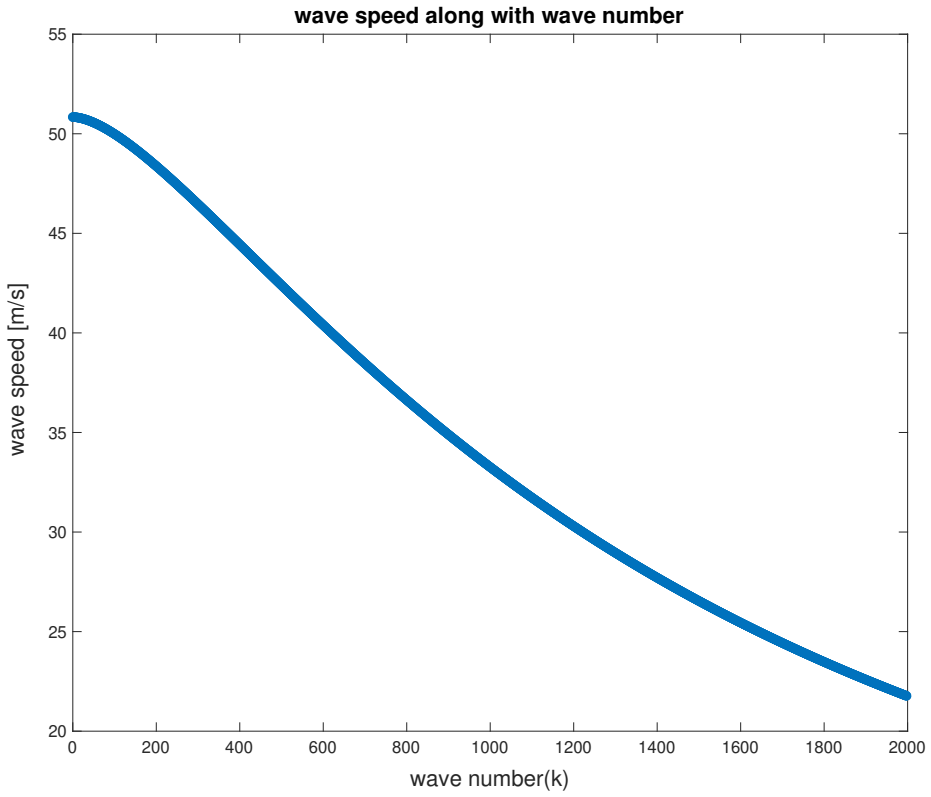

Figure 3.1: Plot of wave speed along with wave numbers, with largest wave speed $c_{wave} \approx 50.81$ m/s.

of the initial conditions is $T_o = 300$ K, $T_b = 290$ K, $T_f = 265$ K, $q_f = 10$ mm, and $q_{tb} = 25$ mm, and other variables are either derived from these or are set to zero. On top of this spatially uniform component is a spatially varying perturbation as described in Fig. 3.2, which helps to initiate waves, cloud clusters, and other weather fluctuations. The spatially varying perturbations were chosen with large-scale wavelengths in both the x and y directions, and with randomly selected amplitudes. For the ocean temperature, the spatially varying perturbation was chosen to have a form that is similar to the prescribed ocean heat transport/forcing term, $F_{merid,o}(x)$.

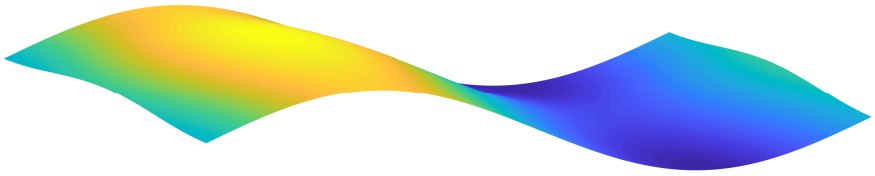

Figure 3.2: Initial perturbation added in model variables' initial condition, with similar form as described in $F_{merid,o}(x)$, consisting of sin/cos waves in zonal and meridional directions respectively.

The most important subroutines we used in simulation is two dimensional discrete Fourier transform (2D-dft) and inverse Fourier transform (2D-idft), which would be used in high frequency during spectrum method, more precisely inside the fluid dynamics solver $\mathcal{A}$ and stochastic solver $\mathcal{B}$. Under the symmetric domain set up, one needs to shift the wave number vector instead of using default fast Fourier transform pattern (**fft2**) directly, which is the algorithm been widely used for functions defined on the domain $[0, 2L_x] \times [0, 2L_y]$, with wave number $k = \{0, \cdots, \frac{N_x}{2} - 1\}$ and $l = \{0, \cdots, \frac{N_y}{2} - 1\}$, here $N_x = L_x/\mathrm{dx}, N_y = L_y/\mathrm{dy}$. One can represent the exact location with given index (m, n) as $x_m = (m-1)\mathrm{dx}, y_n = (n-1)\mathrm{dy}$. Hence according to the Fourier series described in (3.15), the formula of Fourier coefficients under **fft2** are given by

$$\mathbf{fft2}[f](k,l) = \sum_{m=1}^{N_x}\sum_{n=1}^{N_y} f(x_m, y_n) \exp\left[-2\pi i \frac{(k-1)(m-1) + (l-1)(n-1)}{N_x N_y}\right]. \quad (3.62)$$

While in our own set up, the box symmetric domain given by $[-L_x, L_x] \times [-L_y, L_y]$, together with wave number being defined as $k = \{ -\frac{N_x}{2}, -\frac{N_x}{2}+1, \cdots, 0, 1, \cdots, \frac{N_x}{2}-1\}$ and $l = \{ -\frac{N_y}{2}, -\frac{N_y}{2}+1, \cdots, 0, 1, \cdots, \frac{N_y}{2}-1\}$. The representation of physical location will be modified as $x_m = (m - \frac{N_x}{2} - 1)\mathrm{dx}$ and $y_n = (n - \frac{N_y}{2} - 1)\mathrm{dy}$. Thus the Fourier coefficents calculated by shifted 2D-dft algorithm (**sdft2**) are given by

$$\begin{aligned} \mathbf{sdft2}[f](k,l) &= \frac{1}{N_x}\exp\Big[-\pi i\big(k-\frac{N_x}{2}\big)\Big] * \frac{1}{N_y}\exp\Big[-\pi i\big(l-\frac{N_y}{2}\big)\Big] \\ &* \sum_{m=1}^{N_x}\sum_{n=1}^{N_y}(-1)^{m+n} f(x_m, y_n)\exp\Big[-2\pi i\frac{(k-1)(m-1)+(l-1)(n-1)}{N_x N_y}\Big]. \end{aligned} \tag{3.63}$$

Here we define the first part in (3.63) as multiply of two domain scaling factors as

$$\delta_{N_x}(k) = \frac{1}{N_x}\exp\Big[-\pi i\big(k-\frac{N_x}{2}\big)\Big]; \quad \delta_{N_y}(l) = \frac{1}{N_y}\exp\Big[-\pi i\big(l-\frac{N_y}{2}\big)\Big]. \tag{3.64}$$

Noticing that the summation component in (3.63) is just the Fourier coefficients of discrete data $\tilde{f} = (-1)^{m+n} f(x_m, y_n)$ under **fft2**. Hence one can derive **sdft2** coefficients in the form of **fft2** results as

$$\mathbf{sdft2}[f](k,l) = \delta_{N_x}(k) * \delta_{N_y}(l) * \mathbf{fft2}[\tilde{f}](k,l), \tag{3.65}$$

which illustrated that the **sdft2** algorithm can be constructed by multiplying two scale factors with **fft2** result of modified input data.

It is also worth mentioning that when we operate all derivative operators in frequency space by spectrum method, the Fourier coefficients with highest wave number will be zeroed out. More precisely, when $k = -N_x/2$ **or** $l = -N_y/2$, we force that $\hat{\partial}_x(k,l) = \hat{\partial}_y(k,l) = 0$, so that the real constraint would be satisfied and the inverse Fourier transform would always output real type data in physical space. Such technique is widely used in numerical simulation with spectrum method to avoid oscillation induced by large wave number.

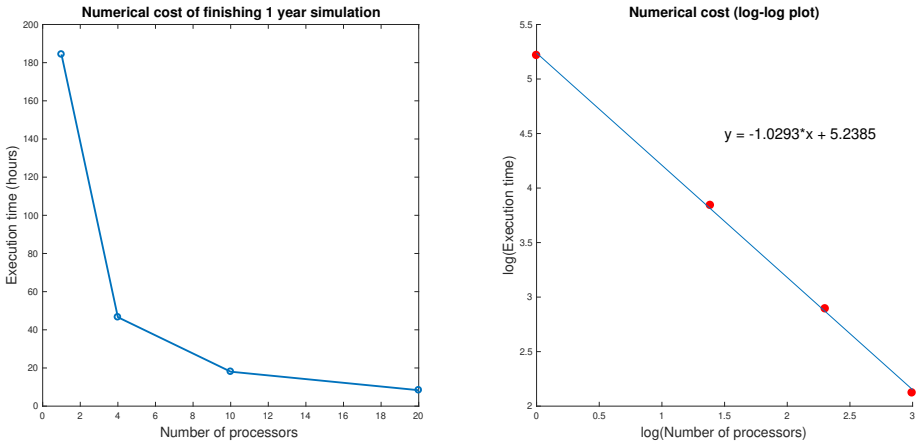

Figure 3.3: Computational cost of unit test under parallel framework, with execution time along with number of processors used given in both scatter and log-log plot, which shows nearly ideal scaling property,

The computer code used for this research program is written in the Fortran programming language, and it is parallelized using message passing interface (MPI). It is based on an earlier parallel code that solves the stochastic heat equation or the quasi-geostrophic (QG) equations using domain decomposition [64]. The parallel framework is extremely efficient when we operate spectrum method and solving ODEs, since every individual Fourier modes is running independently during simulations, and the only communication point between neighbours is contained in Fourier transform / inverse Fourier transform. By using MPI and parallel framework, which makes it possible to obtain simulation results of complicate climate model on fine grid scale within affordable computational cost. We set up an unit test that running the model for one year long under different parallel set up, with execution along with number of processors used given in Fig. (3.3). Under the log-log plot, the ideal scaling of computational cost along with resources proves the efficiency of parallel tools in our numerical method.

Chapter 4

Numerical simulations

Numerical simulations are now presented to investigate the level of realism in the idealized climate system and changes under global warming. The standard parameter values used here are listed above in Tables 2.1–2.4, and other aspects of the setup of the simulations were described above in section 3. In the following chapter, the introduction of simulation with standard parameters and the mean climate state which describes time average data and time evolution of model variables is given in section 4.1; simulation result with increased carbon dioxide quantity and climate change study are illustrated in section 4.2; histogram of rainfall events together with statistics of two cloud types are described in section 4.3; finally sensitivity study of changing cloud parameters is presented in section 4.4.

4.1 Standard simulation and mean climate state

The mean climate statistics are presented in Fig. 4.1. The simulation time was set to 10 years, with the first 6 years serving as a transient period to achieve a statistical equilibrium state, followed by the remaining 4 years for collecting time average data as the mean climate state. The ocean temperature contains a wide western warm pool and eastern

cold pool, induced by the meridional ocean heat transport forcing. The western warm pool region has an excess of moisture quantity in both boundary layer and free troposphere, while the eastern cold pool region has a dearth of moisture and deep convection. These idealizations are consistent with the tropical Pacific Ocean climate. Moreover, the average value and spatial variation of ocean temperature and column water vapor quantity in our model are consistent with natural observation results. Additionally, we obtained reasonable cloud fraction values, with a shallow cloud fraction of approximately 0.5 over the warm pool and a high cloud fraction of 0.8 over the cold pool region as an idealization of a stratocumulus cloud deck. The free tropospheric temperature shows different spatial variation property due to strong diffusion in fluid dynamical process. An important result shown in the mean climate state is the spatial distribution of time average zonal wind velocity, which exhibits a wave-like distribution that is highly consistent with deep convection. This reveals the contribution of spatial divergence in the moisture equation. More precisely, the time average value of zonal wind velocity, which equals over 1 m/s, illustrates that our idealized fluid dynamics has the ability to resolve large scale climate variability such as the Walker circulation.

The model's annual variability is portrayed in Fig. 4.2, wherein the latter half of the 10-year simulation, spanning 5 years, is depicted as a space-time evolution plot that averages variables such as ocean temperature, moisture quantities, and cloud fractions over the meridional direction. This portrayal discloses that the climate state is not a static or forzen equilibrium, but a statistical equilibrium that manifests dynamic evolution and variability in both temporal and spatial dimensions. Seasonal fluctuations are evident in all panels, including variations in cloud fraction that span the entire spectrum of values from 0 to 1. The zonal wind velocity's progression is invariably wave-like and conspicuously accords with that of large, deep convective cloud fraction, thereby corroborating the significance of the Walker circulation in the global moisture-heating balance.

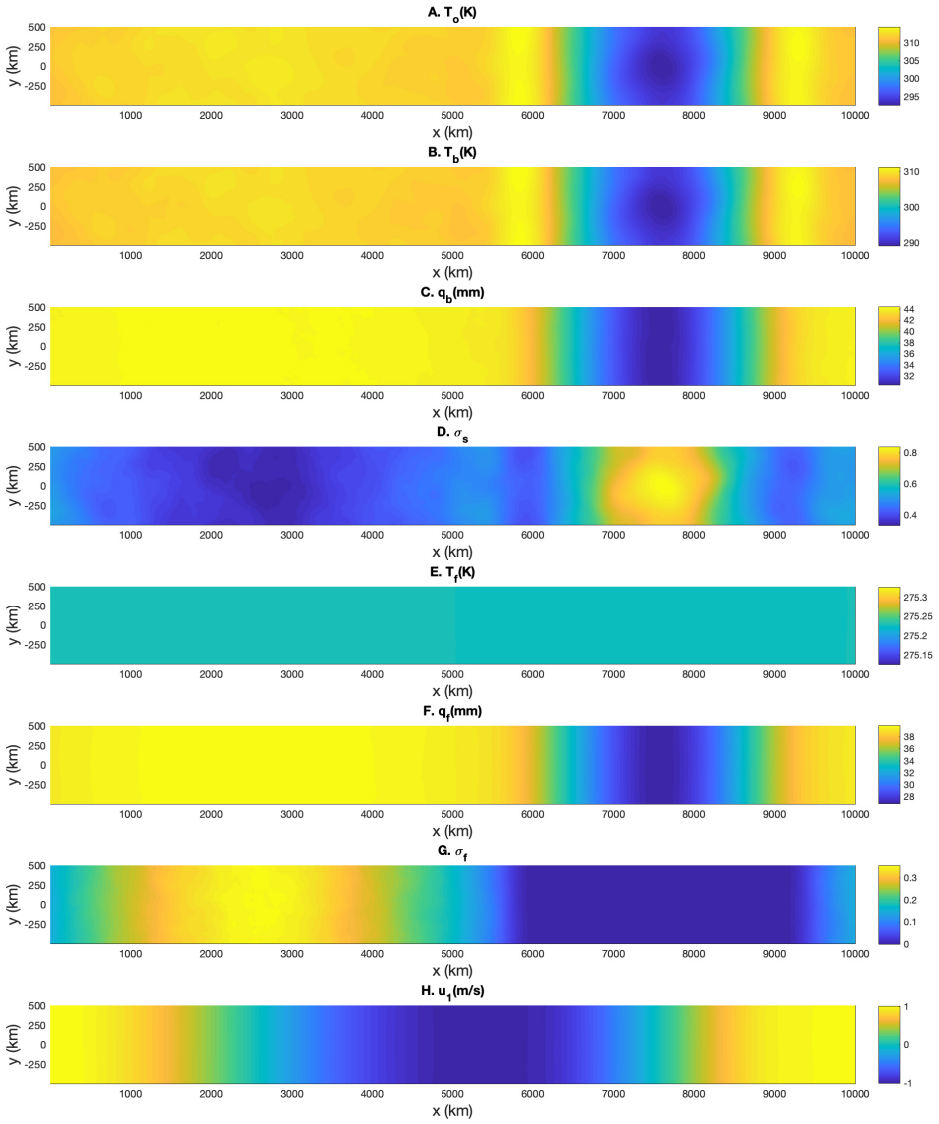

Figure 4.1: The mean climate state (i.e., time-averaged quantities) from simulation with standard parameters. (A) Ocean temperature. (B) Boundary layer temperature. (C) Free-tropospheric temperature. (D) Column water vapor, summation of q_{tb} and q_f. (E) Shallow cloud fraction, from boundary-layer cloud indicator, σ_b. (F) Deep convective cloud fraction, from free-tropospheric cloud indicator, σ_f. (G) First baroclinic mode of zonal wind velocity.

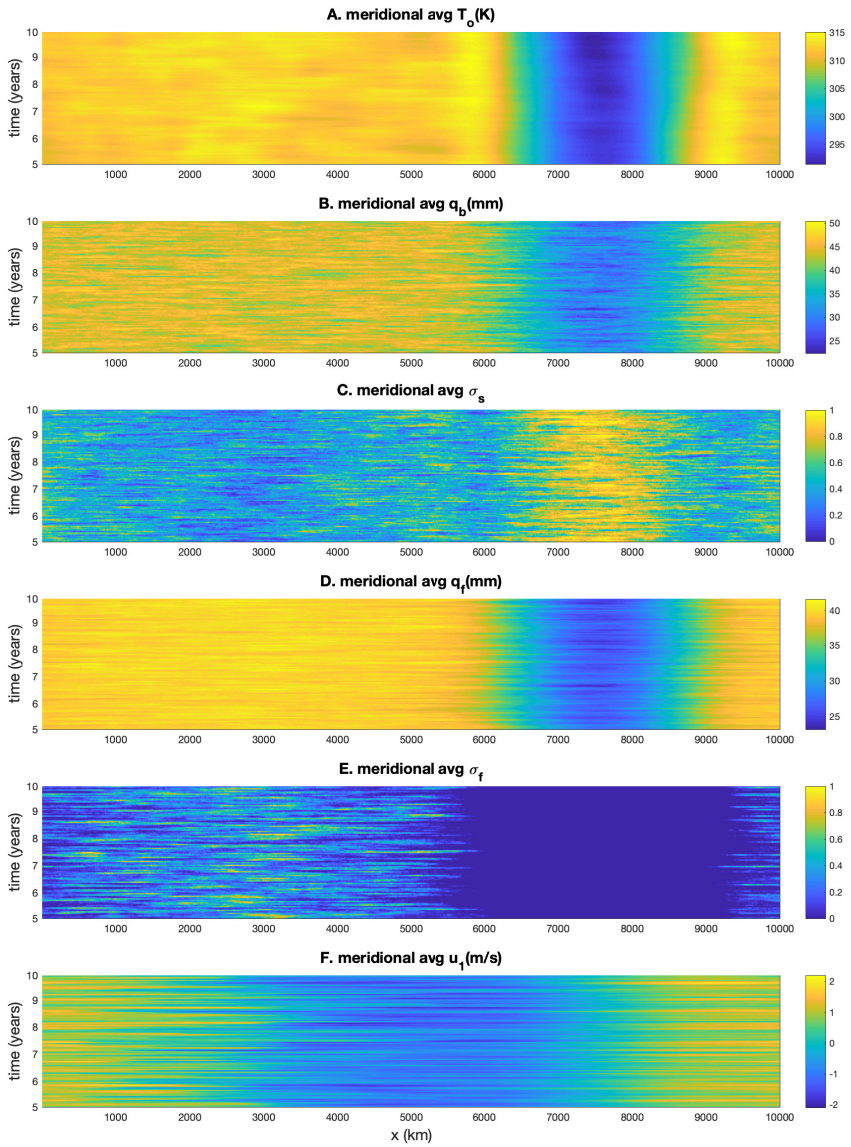

Figure 4.2: Space-and-time evolution plot of model variables (meridionally-averaged) from the simulation with standard parameters during the last 5 years: (A) Ocean temperature. (B) Column water vapor in boundary layer. (C) Shallow cloud fraction. (D) Column water vapor in free troposphere. (E) Deep convective cloud fraction. (F) First baroclinic mode of zonal wind velocity.

4.2 Climate change simulation

In this section, we have undertaken a climate-change experiment to study the impact of an increased carbon dioxide content on the temperature and cloud formations. Specifically, we have formulated a scenario of enhanced carbon dioxide by elevating the longwave absorptivity of both the boundary layer and free troposphere, according to Ref. [37]. In this regard, the absorptivity parameters a_{lb}^0 and a_{lf}^0 were amplified by a factor of 1.4 to attain higher levels of values at $a_{lb}^0 = 0.336$ and $a_{lf}^0 = 0.28$. All other parameters were kept constant, and a new simulation was performed with the same configuration as the standard simulation.

The dissimilarities between the standard simulation and climate-change simulation have been demonstrated via a meridional average plot of the mean climate state, presented in Fig. 4.3. From panels A-C, it is apparent that the ocean and all three layers' temperatures show an increase in their values. Specifically, the ocean temperature has increased by roughly 8 K over the entire domain, whereas the boundary layer and free troposphere temperatures have increased by nearly 4 K and 3.4 K, respectively. Panel D indicates that the column water vapor quantity has surged from 82 mm to 90 mm over the warm pool. Overall, these changes are consistent with the greenhouse gas phenomenon that has been extensively observed during the past decades.

Within the context of the climate-change experiment, significant alterations are observed in the behavior of both types of cloud. The decrease of roughly 0.1 in the shallow cloud fraction over both the warm pool and cool pool is observed in panel E, while panel F indicates a maximum increase of 0.05 in the value of deep convective cloud. Moreover, the transition regions show interesting discrepancies, with the deep convection region displaying a significant increase in its area, while the region with zero deep cloud experiences a decrease of 15% to 20%. Additionally, a notable change in the fraction of deep cloud is evident from the center of the domain towards the core of the cool pool. In the panel displaying shallow cloud fraction, the two valley floors have shifted towards the center

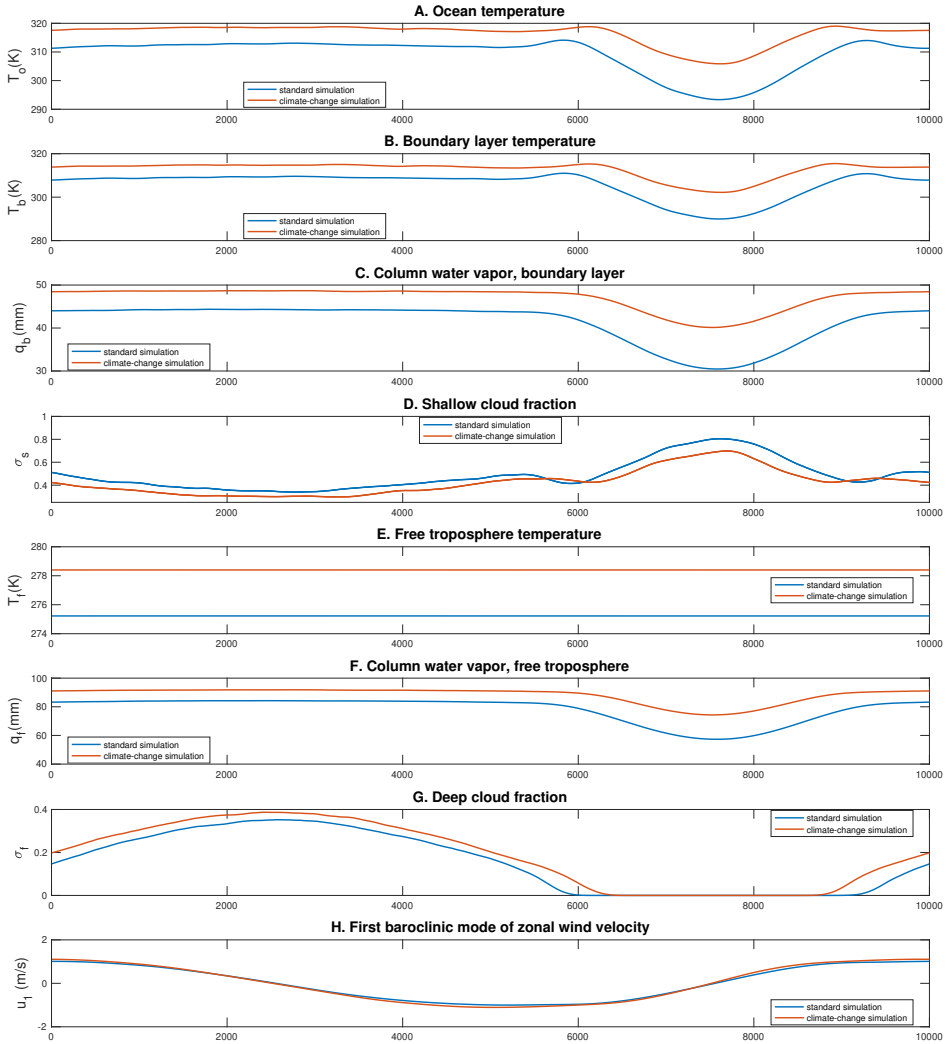

Figure 4.3: The mean climate states in the standard simulation versus climate-change scenario with enhanced longwave absorptivity parameters $a^0_{lb} = 0.336$ and $a^0_{lf} = 0.28$, presented as functions of the zonal coordinate x after time and meridionally averaged. (A) Ocean temperature. (B) Boundary layer temperature. (C) Free-tropospheric temperature. (D) Column water vapor, summation of q_{tb} and q_f. (E) Shallow cloud fraction. (F) Deep convective cloud fraction. (G) Baroclinic mode of zonal wind velocity.

of the cool pool, indicating a reduction in the transient area. Surprisingly, the zonal wind velocity did not exhibit noticeable changes during the climate-change experiment, which is indicative of the stability of the large-scale circulation. Furthermore, these findings align with the evidence from natural phenomena, which suggests that small or inconclusive changes are expected.

The absorption of longwave radiation was increased by a factor of 0.6 and 0.8 in addition to the original factor of 1.4 in the climate-change experiment, with the majority of statistical and feature-based observations remaining highly consistent with those presented in Fig. 4.3. In the event of a decrease in greenhouse gas, one would anticipate cooling across all three layers, a drier atmosphere, and a smaller convection region with higher values of shallow stratocumulus fraction.

4.3 Cloud and rainfall statistics

The essential components of our idealized model are the cloud and rainfall events, and in this section, we present a comprehensive analysis of the basic statistics of both types of clouds along with snapshots. Additionally, we present histogram data of the rainfall events, focusing specifically on the extreme events observed during both standard and climate-change simulations.

Fig. 4.4 showcases snapshots of various deep convective clouds observed during the standard and climate-change scenarios. Panels A and B illustrate the free-tropospheric (deep) cloud indicator, σ_f, of the standard simulation, while panels C and D present σ_f of the climate-change simulation. Panel A and C show snapshots at approximately 9 years, while panels B and D present snapshots at roughly 10 years into the simulation. Upon reviewing all four panels, it becomes apparent that deep convection remains primarily active over the western warm pool region (left part of domain), with a few minor patterns of deep clouds being observed at the left-hand end of the cool pool region (extreme left end of domain). Furthermore, the center of the cool pool region does not exhibit any

convective clouds, which aligns with the fact that the time-averaged σ_f value over the eastern cool pool is zero.

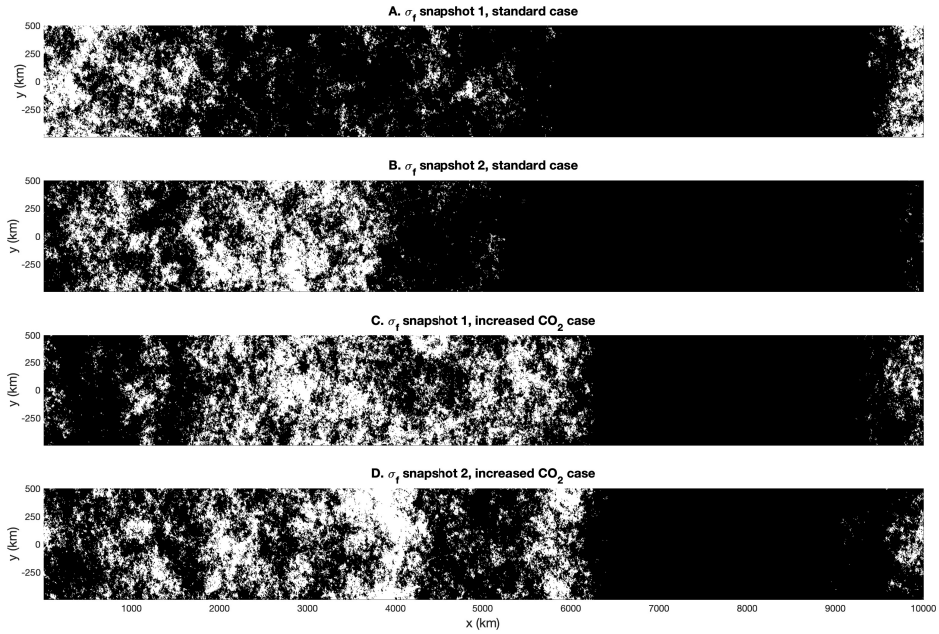

Figure 4.4: Snapshots of deep convective clouds over climate change simulations. Snapshots A and B are taken from standard simulation while C and D are taken from increased carbon dioxide quantity simulation.

From the snapshots shown in Figure 4.4, it is apparent that there has been a rapid increase in the deep cloud fraction and extension of convective region in the climate-change simulation. Comparing panels C-D with panels A-B, it is evident that massive convective clouds have generated over the transient region, which is the region between the warm pool and the cool pool. Additionally, the area of no-convective cloud region has reduced sharply in the climate-change simulation, with the length of such region decreasing from over 4500 km to 3000 km in the snapshots. These observations indicate an increase in rainfall events. To quantify this variation, the raining time and rainfall size statistics were calculated during the simulations by dividing the full domain into 50 km by 50 km boxes and averaging the precipitate inside the box to represent the rainfall quantity. To reduce the noise induced by tiny drizzles (stochastic forcing), lower thresholds were

set in both rain events size and duration statistics. Rain events with a size larger than 0.02 mm and duration longer than 5 minutes were collected, while the maximum values set for closure were 50 mm and 7 days, respectively. The log-log plots of histogram data were created for both events size and duration in Figure 4.5, with all data being normalized and evenly distributed in log scale. In summary, the behavior of both types of statistics matches theoretical properties such as power law and log tail. The standard simulation obtained nearly the same power law scale with climate-change simulation but with a fewer number of tail cases in both two statistics, which agrees with the increase of convective cloud. The fatter log tail of rainfall events in the increased carbon dioxide simulations has been observed by many other models, which is one of the major indicators of simulating the global warming scenario. The slope of event size power law equals 1.51, which is consistent with theoretical results and natural observation data, indicating that our stochastic framework has the potential to simulate deep convection in a natural way.

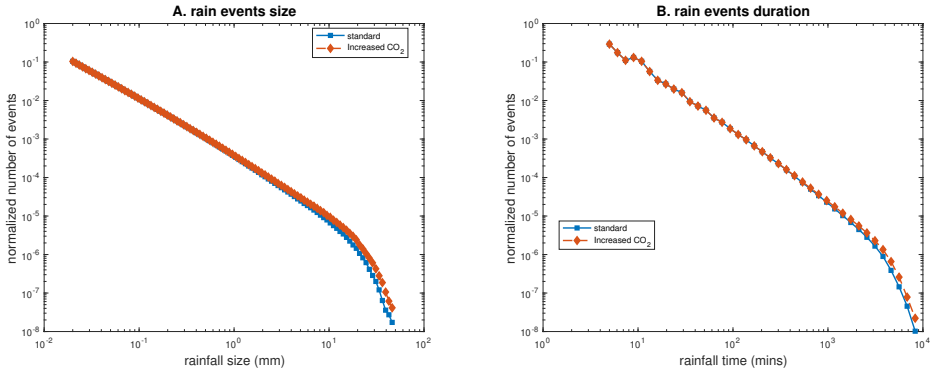

Figure 4.5: Comparison of histogram data of rain events' size and duration, taken over standard simulation and increased carbon dioxide simulation. A: log-log plot of rainfall size's data, lower threshold equals 0.02 mm and upper threshold equals 50 mm, 100 bins used; B: log-log plot of rainfall duration's data, lower threshold equals 5 minutes and upper threshold equals 7 days, 40 bins used.

In Figure 4.4, one can observe cloud clusters of various sizes and spatial distributions. In Panel A, most large-scale clusters are located towards the left end of the warm pool, while in Panels B, C, and D, these clusters are distributed throughout the center of the warm pool. This suggests that the steady state of the system is not a frozen

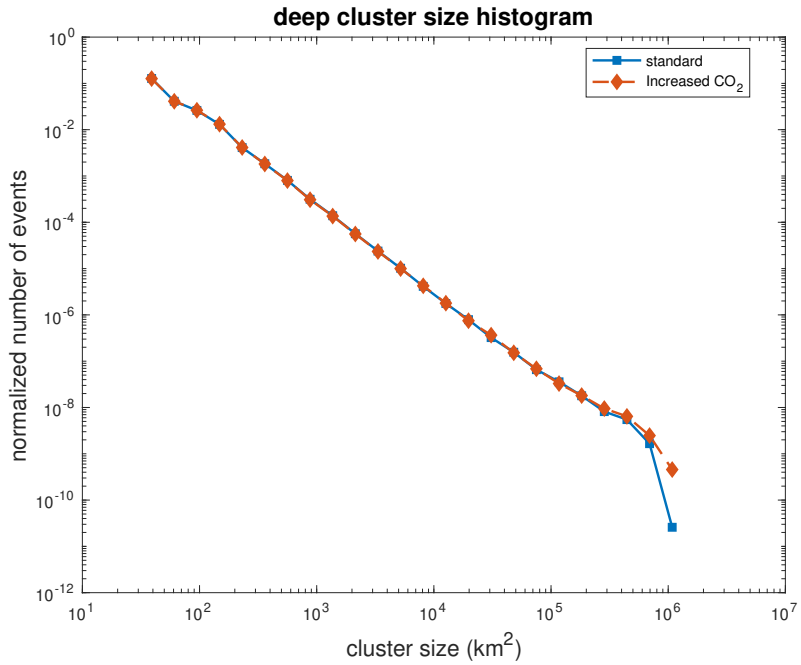

Figure 4.6: log-log plot of histogram data of convective cluster's size, taken over standard simulation and increased carbon dioxide simulation, 30 bins used.

equilibrium, but rather a relatively stable state with moving fluid dynamics. The majority of the clusters have small length scales of approximately O(10) km, although some clusters have larger scales of approximately O(100) km and extend across the entire meridional domain (1000 km). In the climate-change simulation, gigantic deep clusters with sizes of approximately O(1000) km are observed, and the number of large-scale clusters has increased with the enhanced carbon dioxide quantity. In Figure 4.6, we have collected data from over 500 outputs in both standard and climate-change simulations and calculated the size of deep convective clusters. The histogram data is normalized and plotted in log-log form, revealing a power-law scaling. The climate-change case exhibits more extreme large deep clusters in the tail bins. It is noteworthy that the maximum size of the clusters is over one-third of the domain, and such gigantic patterns have also been observed in nature. The increase in the number of large clusters is consistent with the fact that more rainfall events are observed in the climate-change simulation, indicating that our model is capable of simulating the increase in rainfall events under global warming scenarios.

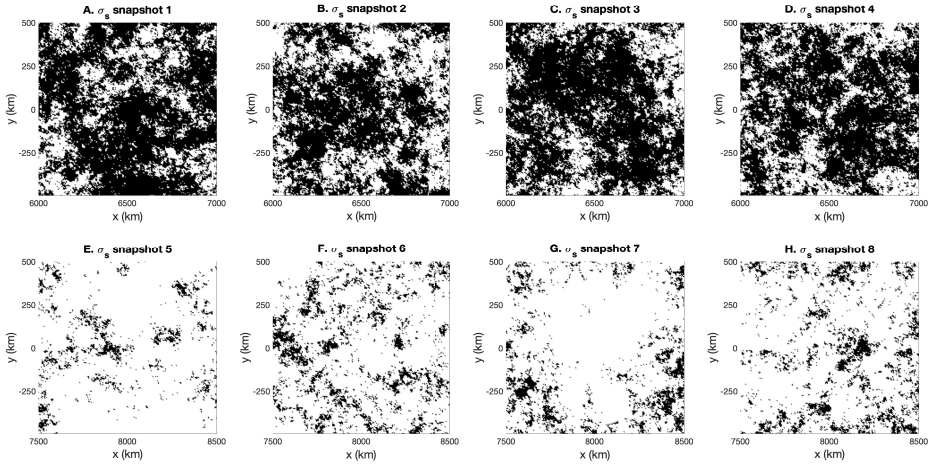

Figure 4.7: Snapshots of shallow cumulus clusters over 1000×1000 km square box, taken at different time steps and different location of the domain. Snapshots A-D are taken over edge of cool pool (5500 to 6500 km in zonal direction) while E-F are taken over core of cool pool (7500 to 8500 km in zonal direction).

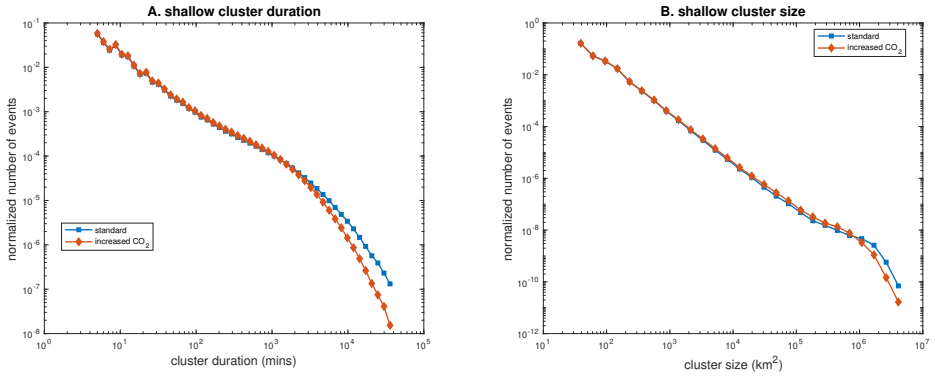

Figure 4.8: Comparison of histogram data of shallow cluster's duration and size, taken over standard simulation and increased carbon dioxide simulation. A: log-log plot of cluster duration's histogram over specific quarter of the domain (6000 to 9000 km), lower threshold equals 10 minutes and upper threshold equals 30 days, 50 bins used; B: log-log plot of cluster size's histogram over the whole domain, 30 bins used.

Figure 4.7 displays snapshots of various shallow clouds obtained from the standard simulation. Panels A to D depict shallow cloud snapshots within a 1000×1000 km box over the transient region (from 5500 to 6500 km in the zonal direction), while panels E to H show snapshots over the center of the cool pool (from 7500 to 8500 km in the zonal direction). Each column of snapshots represents the form of the shallow cumulus cloud at the same time point during the simulation, with the snapshots from column A to D generated at 9, 9.25, 9.5, and 9.75 years, respectively. The differences in the snapshots from the two locations are clear and straightforward, with snapshots taken at the edge of the cool pool having a substantially smaller shallow cloud fraction σ_b than those in the center of the cool pool, consistent with the time-average curve of σ_b from the transient region to the cool pool, as shown in Figure 4.1. As being illustrated in panels E to H, the shallow clouds dissipate and break up into small portions over the transient region, creating an idealization of a stratocumulus cloud deck. Similar portraits of shallow clouds can also be found in related spatiotemporal stochastic cloud models. If we compare all four snapshots in each individual row, differences in cloud shape and seasonal shifts of cloud clusters can be observed. These snapshots illustrate that the idealized model is capable of producing spatiotemporal variation and various life cycles in shallow clouds. The cloud states are not limited by simple fraction numbers, which is one of the advantageous features provided by the new model framework.

In order to provide further insight into the changes in shallow cloud statistics under climate-change simulation, we have collected data on clusters' duration and size and plotted them in a log-log histogram in Fig. 4.8. To describe to most typical behaviours of stratocumulus cloud deck, we only analyzed the duration records of regional clouds over the cool pool, which ranges from 6000 to 9000 km in the zonal direction and is where most large clusters are concentrated. A lower threshold of 10 minutes and an upper threshold of 30 days have been set. Comparison with the histogram data of convection duration reveals that shallow clouds have a longer lifetime than deep convective clouds. As shown in Fig.4.8 A, the data of shallow cloud duration exhibits roughly the same power-law scaling as the

standard simulation, with an increase in greenhouse gas content. However, the number of 'gigantic' clusters with a monthly long lifetime drops significantly. Similar behavior is observed in the cluster size histogram plot, as illustrated in Fig.4.8B, where the short log tail indicates a decrease in the number of giant cumulus clusters. In summary, both types of histogram data are consistent with the mean climate state plot shown in Fig. 4.3. The major feedback of boundary layer clouds to global warming is opposite to that of deep convective clouds, which helps to balance the atmospheric water budget to some extent.

4.4 Sensitivity study

In this section, we conducted several simulations by modifying the values of the shallow cloud albedo $A_b \pm \Delta A_b$ and $A_b \pm 2\Delta A_b$, with an adjustment value of ΔA_b equal to 0.05. All simulations were run for a period of 5 years, with the first 2 years dedicated to reaching an approximate statistical equilibrium, and the last 3 years to collecting time-averaged data, as depicted in the time series plot presented in Fig.4.10. The mean climate state of model variables, i.e., time-averaged data that has been further meridionally-averaged, is displayed in Fig.4.9. The plot indicates that significant changes were primarily induced over the cool pool region, which is intuitive given that most shallow cumulus clusters are formed above that region. Increasing the shallow cloud albedo led to the generation of more shallow clouds at the center of the cool pool, gradually transforming it into a flat region with high shallow fraction values, though not exceeding the maximum value of roughly 0.9. The heavy cloud deck formed over the cool pool further induced the decrease of ocean and boundary layer temperatures, and the low ocean temperatures led to a reduction in the evaporation of sea water. Ultimately, a cool and dry atmospheric environment was formed over the cool pool. Moreover, when we conducted experiments with varied values of A_b, the deep convective statistics and zonal wind velocity retained similar forms as those in the standard simulation, which is consistent with the fact that we only altered the corresponding quantity of the boundary layer.

Regarding the differences observed in the statistics of shallow clouds, as depicted in panel D of Fig. 4.9, it is worth focusing on a specific region ranging from 5500 to 6500 km in the zonal direction, which we refer to as the transient region. The change in the curve of the shallow cloud fraction inside this region is significant. When we conducted simulations with low shallow cloud albedo, the shallow cloud fraction was nearly spatially uniform. However, as we increased the value of A_b, the boundary layer cloud properties underwent obvious variation within the transient interval. Specifically, the shallow cloud fraction increased rapidly in this region as one moved from the western warm pool towards the eastern pool. To provide a more detailed description of the changes observed in shallow cumulus clouds as a function of A_b, we collected histogram data on shallow cloud information over the entire cool pool and plotted it in a log-log format, as illustrated in Fig. 4.11. Based on these two histogram plots, we can gain a better understanding of the changes in shallow cumulus clouds due to the sensitivity of A_b. We found that these shallow clusters had nearly the same cluster size, but some clusters had extremely long duration times. Such longer life-time clusters were likely the main contributor to the increase in the shallow cloud fraction. It is worth noting that the ability of our model framework to provide detailed perspectives on changes in clouds during the exploration of parameter space is also a significant advantage.

In order to conduct a more thorough investigation into the feedback of the free troposphere to cloud parameters, we also performed a sensitivity study on A_f using the same methodology as in the A_b sensitivity test described previously. The comparison of mean climate states is illustrated in Figure 4.12. Surprisingly, significant changes were observed over the eastern cool pool, rather than the warm pool, where deep convection typically occurs. This feedback mechanism can be explained through the heat budget balance of the free troposphere. When A_f is increased, as described in the radiation components (2.51), the convective region would reflect more heating from the free troposphere to other layers. The loss of this source term would indicate a decrease in the temperature T_f over the entire domain. In the cool pool region, in order to maintain

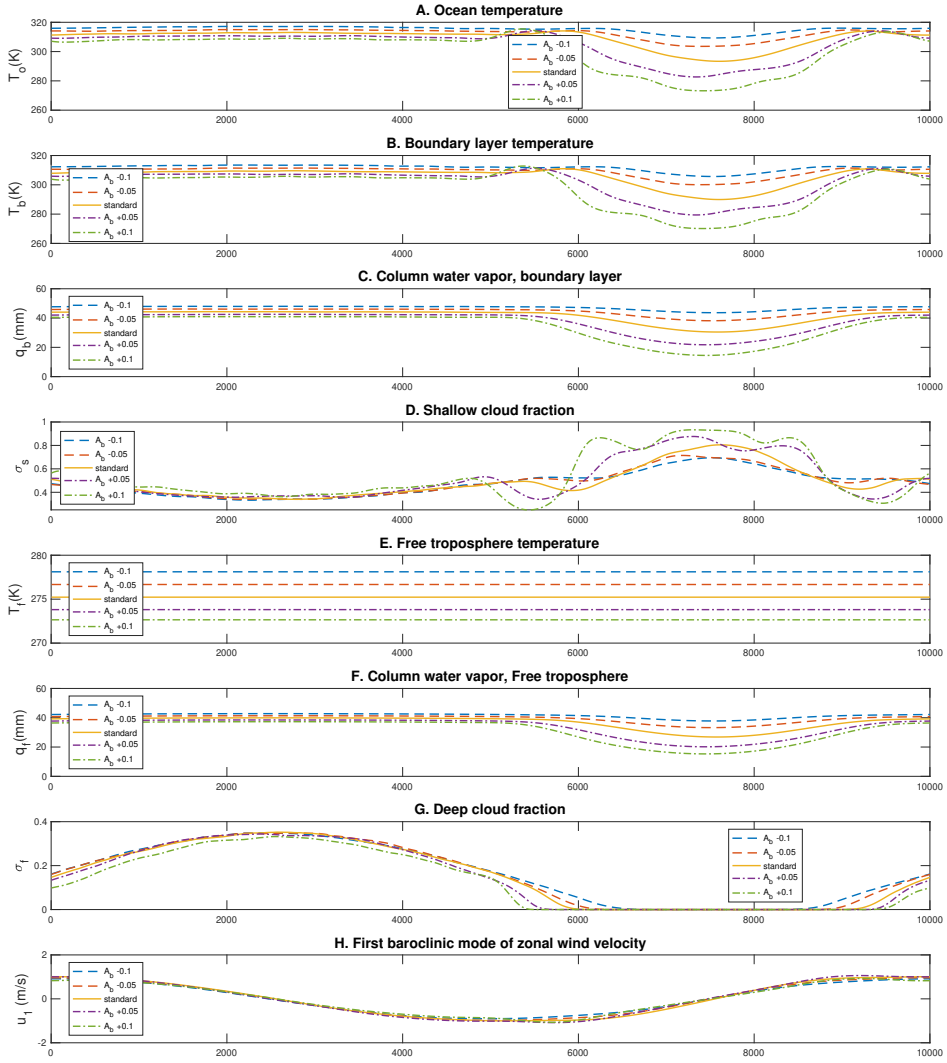

Figure 4.9: Sensitivity study involving shallow cloud albedo parameter A_b. Statistics of model variables are time-averaged and meridionally averaged. Solid lines show the simulation result with standard parameters, dashed lines show results under enhanced shallow cloud albedo, and dash-dot lines show results under reduced shallow cloud albedo. Single adjustment value $\Delta A_b = 0.05$.

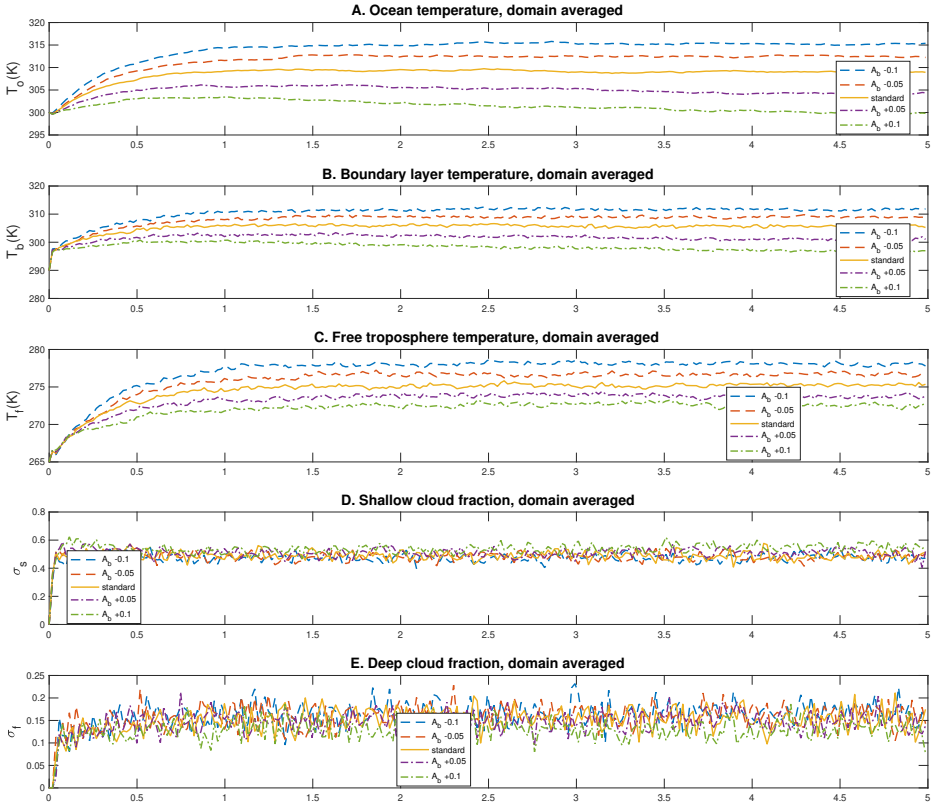

Figure 4.10: Time series of domain-averaged quantities, and comparison between the standard simulation and sensitivity study simulations with various A_b value: (A) Ocean temperature. (B) Boundary layer temperature. (C) Free troposphere temperature. (D) Shallow cloud fraction. (E) Deep cloud fraction.

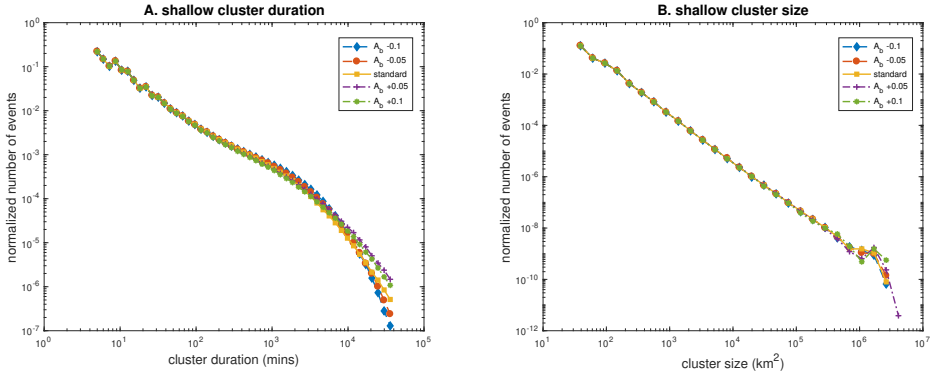

Figure 4.11: Comparison of histogram data of shallow cluster of sensitivity study simulations with various A_b values. All data have been normalized and evenly distributed in log scale: (A) Shallow cluster duration. (B) Shallow cluster size.

the heat equilibrium balance of the θ_1 equation in the absence of deep cloudiness, the only sink term in (2.30) is the spatial divergence. Therefore, a stronger Walker circulation would be induced, resulting in an additional loss of heat over the cool pool.

The enchanced global-scale circulation may entail repercussions on other model variables, such as the amplification of the baroclinic mode of zonal wind velocity curves and the spatial distribution of deep cloudiness. Hypothetically, a stronger Walker circulation would heighten the conveyance of moisture quantities from the western warm pool to the eastern cool pool. Consequently, the augmented divergence term over the cool pool would serve as an additional source of moisture in equation (2.31) for q_f. As illustrated in panel G of Fig. 4.12, the increased convection over the transient region, together with a lower rate of deep cloud fraction over the warm pool and a decrease in the no-convection region would follow suit. Furthermore, according to the moisture feedback in the radiation budget, the augmented water quantities would induce larger parameters of longwave absorptivities through equation (2.52), thereby leading to extra radiative heating in the ocean and boundary layer. This provides an explanation for the elevation of temperatures in these two components.

Another noteworthy feature, as illustrated in Fig. 4.12, is the differential feedback of the circulation for the warm pool and cool regions, with most of the model variables displaying only minor variations over the warm pool. One possible explanation is that, within our framework, the regions without deep convection exhibit greater sensitivity to large-scale circulation. In the presence of deep convective clouds, the cloud clusters can maintain a heat balance through a combination of radiative heating and convective heating. These effects are instrumental in helping the climate system maintain a relatively stable equilibrium, underscoring the crucial role that clouds play in global climate models.

To investigate changes in deep convection more thoroughly, we analyzed the histogram data of rainfall events, as presented in Fig. 4.14. The duration of rainfall events remained nearly same scaling across simulations with varying A_f values. Furthermore, the

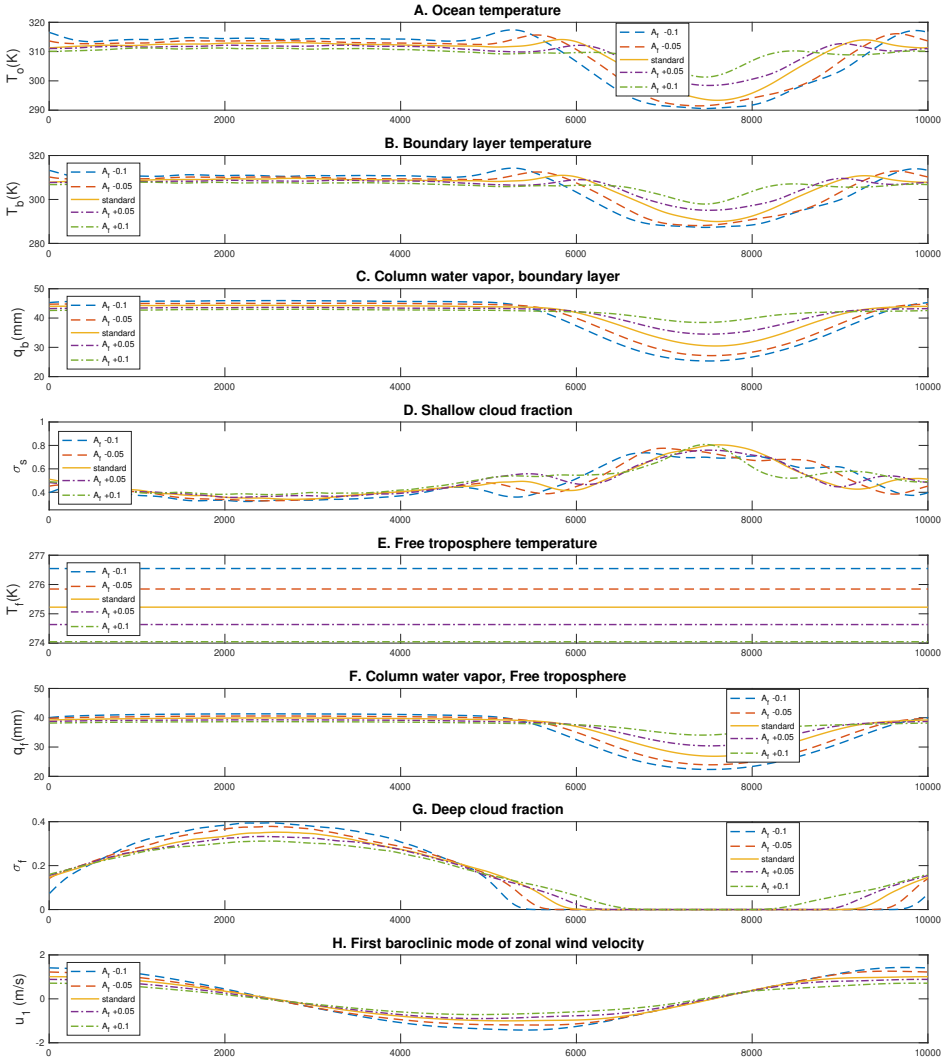

Figure 4.12: Sensitivity study involving deep cloud albedo parameter A_f. Statistics of model variables are time-averaged and meridionally averaged. Solid lines show the simulation result with standard parameters, dashed lines show results under enhanced deep cloud albedo, and dash-dot lines show results under reduced deep cloud albedo. Single adjustment value $\Delta A_f = 0.05$.

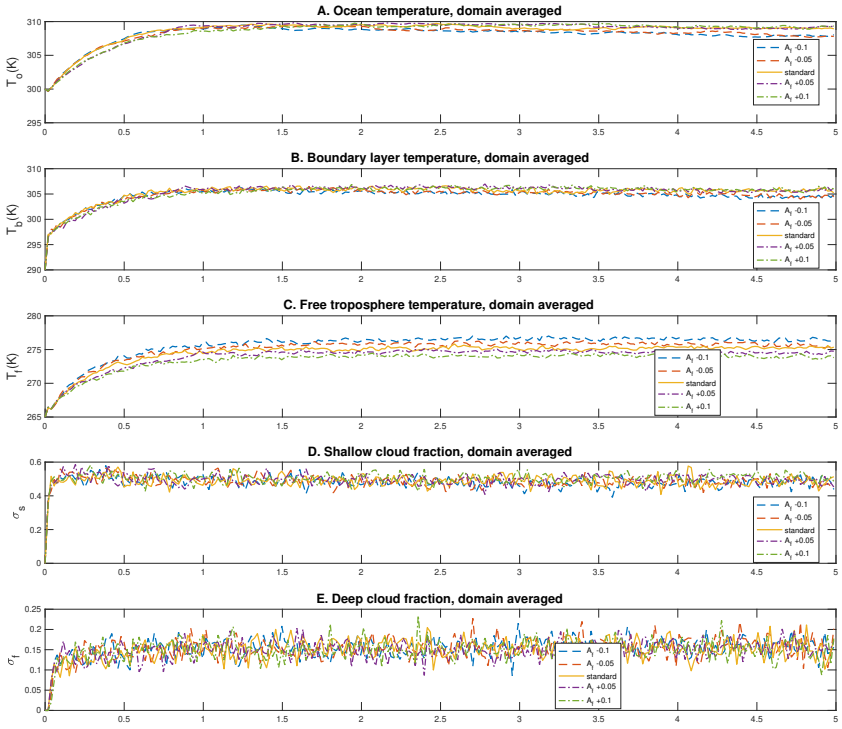

Figure 4.13: Time series of domain-averaged quantities, and comparison between the standard simulation and sensitivity study simulations with various A_f value: (A) Ocean temperature. (B) Boundary layer temperature. (C) Free troposphere temperature. (D) Shallow cloud fraction. (E) Deep cloud fraction.

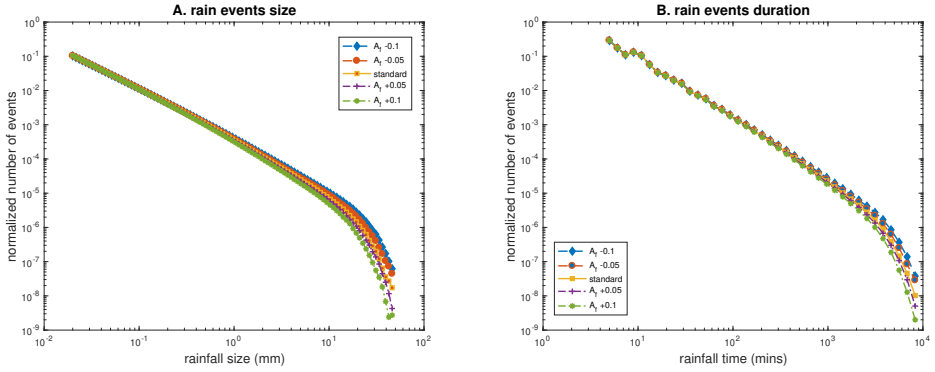

Figure 4.14: Comparison of histogram data of deep convection of sensitivity study simulations with various A_b values. All data have been normalized and evenly distributed in log scale: (A) rain events size. (B) rain events duration.

increase in deep cloud albedo resulted in a reduction of extreme events, consistent with the decrease in deep cloud fraction values over the warm pool, where large-scale rainfall and storms often occur.

In summary, changes in deep cloud albedo A_f can impact the climate system by inducing stronger large-scale circulation and further altering the inner spatial variation of certain physical variables over the zonal direction. After spatial averaging, as demonstrated in the time series plot in Fig.4.13, most statistics underwent only slight fluctuations, rather than significant changes observed in Fig.4.10. These inner changes were captured through the coupling of different layers and the moist-temperature relationship, such as the temperature dependence in moist thresholds and moist feedback in radiation parameters. This highlights one of the most important features of our multiple layers' model, demonstrating that each layer is not an individual component but a fully-coupled climate system with internal dynamics.

Chapter 5

Conclusion

In this thesis, we have presented a comprehensive framework for modeling idealized climate simulations with the presence of stratocumulus clouds and convection within a planetary-scale domain. Our approach integrates a large-scale fluid dynamics model that is capable of resolving climate variability, such as the Walker circulation, with spatiotemporal stochastic models that capture the small-scale turbulent advection-diffusion of water vapor and cumulus clouds. Through our numerical simulations, we have obtained the mean climate state with basic regional differences, which reveals a western warm-pool region characterized by prominent deep convective clouds, and an eastern cold-pool region characterized by an expansive stratocumulus cloud deck with barely any deep convection. Moreover, we have investigated the basic features of climate-change scenarios, such as changes in global temperatures, water vapor quantities, and cloud fractions under different climate equilibrium. Our results are illustrated through simple models, and provide valuable insights into the potential impacts of climate change on the distribution and behavior of stratocumulus clouds and convection within a planetary-scale domain.

Aside from the bulk-averaged cloud properties, such as area fractions, we have conducted a more in-depth investigation into individual cloud statistics. Specifically, we

have quantified rainfall events over the entire domain through histogram data plotted under log-log scales. This approach allowed us to illustrate the cloud-radiative feedback processes related to these individual properties. Our analysis includes the power-law distribution of both rain event size and convective cluster area, with slope values that closely match theoretical predictions. Notably, our results show relatively good agreement with observations, despite the simplicity of our model. Furthermore, we have examined the changes in extreme events under different global warming scenarios and the sensitivity of these events to cloud processes. By comparing different tail effects, we have revealed a more frequent occurrence of extreme events with increasing levels of carbon dioxide, indicating that the upsurge of greenhouse gas would also increase the turbulent variability in our model.

In our study, we have not only examined deep convective clouds, but also investigated the statistics of stratocumulus cloud decks. To this end, we have designed histogram plots of both cluster lifetime and size. To provide a more accurate representation of the changes in shallow cloud decks under different climate situations, such as varying CO2 quantities, cloud albedo, or aerosols, we have collected regional histogram data solely over the center of the cold pool. Our findings reveal similar power-law distributions with different power tails, which suggests that the dynamics of living shallow clusters generated by our simple stochastic model play a crucial role in global climate variability. This positive feedback highlights the need to consider many other questions and extensions in the future, such as the effects of aerosols, interactive albedo, and a wider variety of cloud types.

Finally, during our sensitivity studies, we have observed significant changes in climate-scale circulations. Specifically, the fluctuations in the first baroclinic mode of zonal wind velocity have indicated the feedback of Walker circulation in response to changes in cloud processes. These feedbacks have induced obvious impacts on thermodynamic variables across all layers and have highlighted the complexity of inner dynamics in our simple model. It is important to note that our variables are not simulated individually

but are coupled with other related components to resolve climate variability. In future research, it would be interesting to explore the inner relationships between parameters by adding more processes, such as stochastic entrainments or nonlinearity in fluid dynamics. Incorporating these extra components may help us better understand the changes in large-scale circulations and corresponding fluctuations.

Bibliography

[1] G. W. Petty. *A first course in atmospheric radiation*. Sundog Pub, Madison, Wisconsin, USA, 2006.

[2] J David Neelin. *Climate change and climate modeling*. Cambridge University Press, New York, 2010.

[3] IPCC. *Climate Change 2013: The Physical Science Basis. Working Group I Contribution to the Fifth Assessment Report of the Intergovernmental Panel on Climate Change*. Ed. by T.F. Stocker et al. Cambridge University Press, New York, 2013.

[4] R. D. Cess et al. "Intercomparison and interpretation of climate feedback processes in 19 atmospheric general circulation models". In: *J. Geophys. Res.* 95.D10 (1990), pp. 16601–16615. DOI: 10.1029/JD095iD10p16601.

[5] G. L. Stephens. "Cloud feedbacks in the climate system: A critical review". In: *J. Climate* 18.2 (2005), pp. 237–273.

[6] S. Bony and J.L. Dufresne. "Marine boundary layer clouds at the heart of tropical cloud feedback uncertainties in climate models". In: *Geophys. Res. Lett* 32 (2005), p. 20806.

[7] Sandrine Bony et al. "Clouds, circulation and climate sensitivity". In: *Nature Geoscience* 8.4 (2015), p. 261.

[8] B. Stevens. "Atmospheric moist convection". In: *Annu. Rev. Earth Planet. Sci.* 33.1 (2005), pp. 605–643.

[9] B. Stevens et al. "Evaluation of large-eddy simulations via observations of nocturnal marine stratocumulus". In: *Mon. Wea. Rev.* 133.6 (2005), pp. 1443–1462.

[10] S. N. Stechmann. "Multiscale eddy simulation for moist atmospheric convection: Preliminary investigation". In: *J. Comput. Phys.* 271 (2014), pp. 99–117.

[11] Georgios Matheou, Daniel Chung, and João Teixeira. "Large-eddy simulation of a stratocumulus cloud". In: *Physical Review Fluids* 2.9 (2017), p. 090509.

[12] Juan Pedro Mellado. "Cloud-top entrainment in stratocumulus clouds". In: *Annual Review of Fluid Mechanics* 49 (2017), pp. 145–169.

[13] S. N. Stechmann and H. R. Ogrosky. "The Walker circulation, diabatic heating, and outgoing longwave radiation". In: *Geophys. Res. Lett.* 41 (2014), pp. 9097–9105. DOI: 10.1002/2014GL062257.

[14] Eui-Seok Chung et al. "Reconciling opposing Walker circulation trends in observations and model projections". In: *Nature Climate Change* 9.5 (2019), pp. 405–412.

[15] Caroline J Muller, Paul A O'Gorman, and Larissa E Back. "Intensification of precipitation extremes with warming in a cloud-resolving model". In: *Journal of Climate* 24.11 (2011), pp. 2784–2800.

[16] David M Romps. "Response of tropical precipitation to global warming". In: *Journal of the Atmospheric Sciences* 68.1 (2011), pp. 123–138.

[17] MF Khairoutdinov and C-E Yang. "Cloud-resolving modelling of aerosol indirect effects in idealised radiative-convective equilibrium with interactive and fixed sea surface temperature". In: *Atmospheric Chemistry and Physics* 13.8 (2013), pp. 4133–4144.

[18] Caroline Muller and Yukari Takayabu. "Response of precipitation extremes to warming: what have we learned from theory and idealized cloud-resolving simulations, and what remains to be learned?" In: *Environmental Research Letters* 15.3 (2020), p. 035001.

[19] Christopher S Bretherton. "Challenges in numerical modeling of tropical circulations". In: *The Global Circulation of the Atmosphere*. Ed. by Tapio Schneider and Adam H. Sobel. Princeton University Press, Princeton, 2007. Chap. 11, pp. 302–330.

[20] W. W. Grabowski and P. K. Smolarkiewicz. "CRCP: a Cloud Resolving Convection Parameterization for modeling the tropical convecting atmosphere". In: *Physica D: Nonlinear Phenomena* 133 (1999), pp. 171–178.

[21] S. Hottovy and S. N. Stechmann. "A spatiotemporal stochastic model for tropical precipitation and water vapor dynamics". In: *J. Atmos. Sci.* 72 (2015), pp. 4721–4738. DOI: 10.1175/JAS-D-15-0119.1.

[22] S. N. Stechmann and S. Hottovy. "Cloud regimes as phase transitions". In: *Geophys. Res. Lett.* 43 (2016), pp. 6579–6587. DOI: 10.1002/2016GL069396.

[23] Fiaz Ahmed and J David Neelin. "Explaining scales and statistics of tropical precipitation clusters with a stochastic model". In: *Journal of the Atmospheric Sciences* 76.10 (2019), pp. 3063–3087.

[24] Boualem Khouider and Alexander Bihlo. "A new stochastic model for the boundary layer clouds and stratocumulus phase transition regimes: Open cells, closed cells, and convective rolls". In: *Journal of Geophysical Research: Atmospheres* 124.1 (2019), pp. 367–386.

[25] Diana L Monroy and Gerardo G Naumis. "Description of mesoscale pattern formation in shallow convective cloud fields by using time-dependent Ginzburg-Landau and Swift-Hohenberg stochastic equations". In: *Physical Review E* 103.3 (2021), p. 032312.

[26] J. David Neelin and Ning Zeng. "A quasi-equilibrium tropical circulation model—formulation". In: *J. Atmos. Sci.* 57 (2000), pp. 1741–1766.

[27] J.W.B. Lin and J.D. Neelin. "Influence of a stochastic moist convective parameterization on tropical climate variability". In: *Geophys. Res. Lett.* 27.22 (2000), pp. 3691–3694. DOI: 10.1029/2000GL011964.

[28] B. Khouider and A. J. Majda. "A non-oscillatory balanced scheme for an idealized tropical climate model: Part I: Algorithm and validation". In: *Theor. Comp. Fluid Dyn.* 19.5 (2005), pp. 331–354.

[29] B. Khouider and A. J. Majda. "Multicloud convective parameterizations with crude vertical structure". In: *Theor. Comp. Fluid Dyn.* 20 (2006), pp. 351–375.

[30] B. Khouider, J. A. Biello, and A. J. Majda. "A stochastic multicloud model for tropical convection". In: *Comm. Math. Sci.* 8 (2010), pp. 187–216.

[31] Y. Frenkel, A. J. Majda, and S. N. Stechmann. "Cloud-radiation feedback and atmosphere-ocean coupling in a stochastic multicloud model". In: *Dyn. Atmos. Oceans* 71 (2015), pp. 35–55. DOI: 10.1016/j.dynatmoce.2015.05.003.

[32] Y. Chen and S. N. Stechmann. "Multi-model communication and data assimilation for mitigating model error and improving forecasts". In: *Chin. Ann. Math. Ser. B* 40 (2019), pp. 689–720.

[33] A. J. Majda. *Introduction to PDEs and Waves for the Atmosphere and Ocean.* Vol. 9. Courant Lecture Notes in Mathematics. Providence: American Mathematical Society, 2003, pp. x+234. ISBN: 0-8218-2954-8.

[34] S. N. Stechmann, A. J. Majda, and B. Khouider. "Nonlinear dynamics of hydrostatic internal gravity waves". In: *Theor. Comp. Fluid Dyn.* 22 (2008), pp. 407–432.

[35] M. L. Waite and B. Khouider. "Boundary layer dynamics in a simple model for convectively coupled gravity waves". In: *J. Atmos. Sci.* 66.9 (2009), pp. 2780–2795.

[36] M. A. Kelly and D. A. Randall. "A two-box model of a zonal atmospheric circulation in the Tropics". In: *J. Climate* 14.19 (2001), pp. 3944–3964.

[37] Eli A Mueller and Samuel N Stechmann. "Shallow-cloud impact on climate and uncertainty: A simple stochastic model". In: *Mathematics of Climate and Weather Forecasting* 6.1 (2020), pp. 16–37. DOI: 10.1515/mcwf-2020-0002.

[38] Roger Marchand and Thomas Ackerman. "A cloud-resolving model with an adaptive vertical grid for boundary layer clouds". In: *Journal of the atmospheric sciences* 68.5 (2011), pp. 1058–1074.

[39] Wojciech W Grabowski. "Towards global large eddy simulation: Super-parameterization revisited". In: *Journal of the Meteorological Society of Japan. Ser. II* 94 (2016), pp. 327–344.

[40] Hossein Parishani et al. "Toward low-cloud-permitting cloud superparameterization with explicit boundary layer turbulence". In: *Journal of Advances in Modeling Earth Systems* 9.3 (2017), pp. 1542–1571.

[41] David H Marsico and Samuel N Stechmann. "Expanding grids for efficient cloud dynamics simulations across scales". In: *Mathematics of Climate and Weather Forecasting* 6.1 (2020), pp. 38–49. DOI: 10.1515/mcwf-2020-0101.

[42] Adam H Sobel and J David Neelin. "The boundary layer contribution to intertropical convergence zones in the quasi-equilibrium tropical circulation model framework". In: *Theoretical and Computational Fluid Dynamics* 20.5 (2006), pp. 323–350.

[43] B. Stevens. "Bulk boundary-layer concepts for simplified models of tropical dynamics". In: *Theor. Comp. Fluid Dyn.* 20.5 (2006), pp. 279–304.

[44] S. N. Stechmann and S. Hottovy. "Unified spectrum of tropical rainfall and waves in a simple stochastic model". In: *Geophys. Res. Lett.* 44 (2017), pp. 10, 713–10, 724. DOI: 10.1002/2017GL075754.

[45] J. A. Biello and A. J. Majda. "Boundary layer dissipation and the nonlinear interaction of equatorial baroclinic and barotropic Rossby waves". In: *Geophys. Astrophys. Fluid Dynam.* 98 (Feb. 2004), pp. 85–127.

[46] R. Neggers, B. Stevens, and J.D. Neelin. "A simple equilibrium model for shallow-cumulus-topped mixed layers". In: *Theoretical and Computational Fluid Dynamics* 20.5 (2006), pp. 305–322.

[47] N. A. Phillips. “Energy transformations and meridional circulations associated with simple baroclinic waves in a two-level, quasi-geostrophic model”. In: *Tellus* 6.3 (1954), pp. 273–286.

[48] Norman A Phillips. “The general circulation of the atmosphere: A numerical experiment”. In: *Quarterly Journal of the Royal Meteorological Society* 82.352 (1956), pp. 123–164.

[49] Isaac M Held. “The gap between simulation and understanding in climate modeling”. In: *Bulletin of the American Meteorological Society* 86.11 (2005), pp. 1609–1614.

[50] G.K. Vallis. *Atmospheric and Oceanic Fluid Dynamics: Fundamentals and Large-scale Circulation*. New York: Cambridge University Press, 2006.

[51] R. Hu et al. “Initial investigations of precipitating quasi-geostrophic turbulence with phase changes”. In: *Research in the Mathematical Sciences* 8.6 (2021). DOI: https://doi.org/10.1007/s40687-020-00242-3.

[52] Brian E. Mapes and Robert A. Houze Jr. “Diabatic divergence profiles in western Pacific mesoscale convective systems”. In: *J. Atmos. Sci.* 52 (1995), pp. 1807–1828.

[53] G. N. Kiladis et al. “Convectively coupled equatorial waves”. In: *Rev. Geophys.* 47 (2009), RG2003. DOI: 10.1029/2008RG000266.

[54] R.R. Rogers and M.K. Yau. *A short course in cloud physics*. Butterworth–Heinemann, Burlington, 1989.

[55] J. D. Neelin, O. Peters, and K. Hales. “The transition to strong convection”. In: *J. Atmos. Sci.* 66.8 (2009), pp. 2367–2384.

[56] R. Salmon. *Lectures on Geophysical Fluid Dynamics*. New York: Oxford University Press, 1998.

[57] A. J. Majda and P. R. Kramer. “Simplified models for turbulent diffusion: theory, numerical modelling, and physical phenomena”. In: *Phys. Rep.* 314.4 (1999), pp. 237–574. DOI: 10.1016/S0370-1573(98)00083-0.

[58] T. DelSole. “Stochastic models of quasigeostrophic turbulence”. In: *Surv. Geophys.* 25.2 (2004), pp. 107–149. DOI: 10.1023/B:GEOP.0000028160.75549.0d.

[59] A. J. Majda and M. J. Grote. “Explicit off-line criteria for stable accurate time filtering of strongly unstable spatially extended systems”. In: *Proc. Natl. Acad. Sci. USA* 104 (2007), pp. 1124–1129.

[60] A. J. Majda and M. J. Grote. “Mathematical test models for superparametrization in anisotropic turbulence”. In: *Proc. Natl. Acad. Sci. USA* 106.14 (2009), pp. 5470–5474.

[61] W. W. Grabowski and P. K. Smolarkiewicz. “Two-time-level semi-Lagrangian modeling of precipitating clouds”. In: *Mon. Wea. Rev.* 124.3 (1996), pp. 487–497.

[62] Matthew E. Peters and Christopher S. Bretherton. “A simplified model of the Walker circulation with an interactive ocean mixed layer and cloud–radiative feedbacks”. In: *J. Climate* 18 (2005), pp. 4216–4234.

[63] C. W. Gardiner. *Handbook of stochastic methods: for physics, chemistry & the natural sciences*. Vol. 13. Springer Series in Synergetics. Springer–Verlag, Berlin, 2004.

[64] Jason L. Torchinsky and Samuel N. Stechmann. *EZ Parallel version 1.0*. Github Repository. 2020. DOI: 10.5281/zenodo.4107203. URL: https://www.doi.org/10.5281/zenodo.4107203.